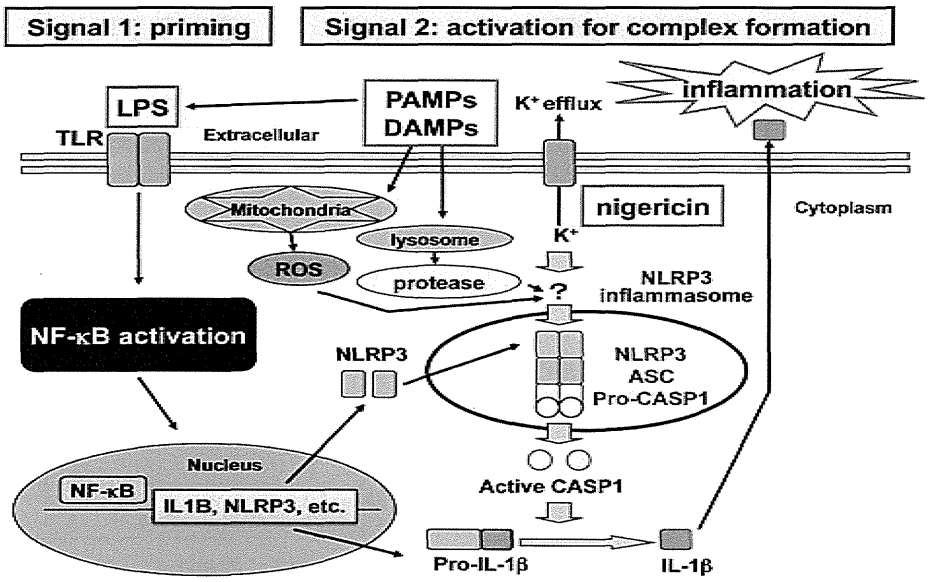

Figure 1: Two-step signals for NLRP3 inflammasome activation. Activation of NLRP3 inflammasome, composed of NLRP3, ASC, and pro-CASP1, is tightly regulated by two-step signals. The first "priming" signal, such as LPS, enhances the expression of inflammasome components and target proteins via activation of transcription factor NF-κB. The second "activation" signal promotes the assembly of inflammasome components. The second signal involves three major mechanisms, including generation of ROS, lysosomal damage, and the potassium efflux. Abbreviations: LPS, lipopolysaccharide; TLR, toll-like receptor; PAMPs, pathogen-associated molecular patterns; DAMPs, danger-associated molecular patterns; ROS, reactive oxygen species.

mitochondrial DNA directly activates NLRP3 inflammasome following induction of apoptosis [6]. By serving as an inducer of two-step signals, a diverse range of danger signals armed with PAMPs, such as *Listeria monocytogenes*, *Candida albicans*, and influenza A virus and those with DAMPs, such as amyloid-β (Aβ), uric acid and cholesterol crystals, asbestos, silica, alum, hyaluronan, and adenosine 5'-triphosphate (ATP), promptly activate the NLRP3 inflammasome [7,8].

Deregulated activation of NLRP3 inflammasome contributes to the pathological processes of various diseases, such as type 2 diabetes, Alzheimer's disease (AD), and multiple sclerosis (MS) [9-11]. Lack of NLRP3 inflammasome components skews microglial cells to an anti-inflammatory M2 phenotype with an enhanced capacity of amyloid-β (Aβ) clearance in a mouse model of AD [10]. *Nlrp3*-knockout mice showed reduced severity of experimental autoimmune encephalomyelitis (EAE), a mouse model of MS, characterized by substantial attenuation of inflammation, demyelination and astrogliosis [12]. In active inflammatory demyelinating lesions of MS, reactive astrocytes and perivascular macrophages expressed all three components of NLRP3 inflammasome, such as NLRP3, ASC, and CASP1, along with IL-1β, suggesting that biochemical agents and monoclonal antibodies designed to block specifically NLRP3 inflammasome activation might be highly effective in treatment of active MS [11]. However, at present, the precise mechanism regulating NLRP3 inflammasome activation and deactivation remains largely unknown. In the present study, by genome-wide gene expression profiling, we attempts to clarify the comprehensive molecular network of NLRP3 inflammasome activation-responsive genes in a human monocyte cell line given consecutively two-step signals.

Materials and Methods

NLRP3 inflammasome activation

A human monocyte cell line THP-1 was obtained from RIKEN Cell Bank (Saitama, Japan). The cells were maintained in RPMI 1640 medium (Invitrogen, Carlsbad, CA, USA) supplemented with 10% fetal bovine serum (FBS), 55 μM 2-mercaptoethanol, 2 mM L-glutamine, 100 U/ml penicillin and 100 μg/ml streptomycin (feeding medium). To load the Signal 1, the cells were incubated for 3 hours with or without 0.2 μg/ml lipopolysaccharide (LPS; Sigma, St. Louis, MO, USA). To load the Signal 2, they were washed twice by Phosphate-Buffered Saline (PBS) and incubated further for 0.5 or 2 hours with 10 μM nigericin sodium salt (Wako Pure Chemical, Osaka, Japan) dissolved in ethanol or the equal v/v% concentration of ethanol (vehicle). Then, protein extract of the cells was processed for western blot analysis with a rabbit antibody against the C-terminal peptide of the human CASP1 p10 protein (sc-515, Santa Cruz Biotechnology, Santa Cruz, CA, USA) and a rabbit antibody against the peptide mapping at amino acid residues of 117-269 of the human IL-1β protein (sc-7884, Santa Cruz Biotechnology).

Microarray analysis

Total cellular RNA was isolated by using the TRIZOL plus RNA Purification kit (Invitrogen). The quality of total RNA was evaluated on Agilent 2100 Bioanalyzer (Agilent Technologies, Palo Alto, CA, USA). Three hundred ng of total RNA was processed for cDNA synthesis, fragmentation, and terminal labeling with the GeneChip Whole Transcript Sense Target Labeling and Control Reagents (Affymetrix, Santa Clara, CA, USA). Then, the labeled cRNA was processed for hybridization at 45°C for 17 hours with Human Gene 1.0 ST Array (28,869 genes; Affymetrix). The arrays were washed in the

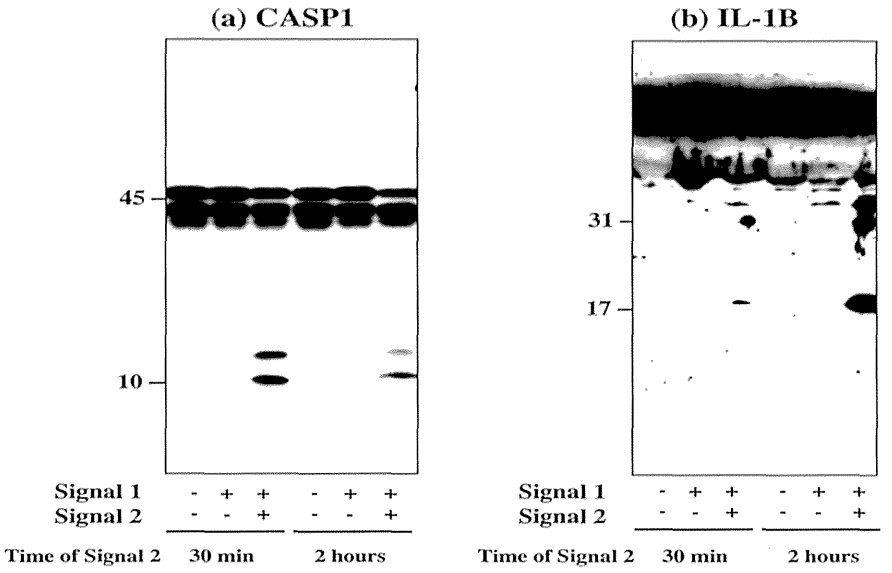

Figure 2: Two-step signals activate NLRP3 inflammasome in THP-1 cells. NLRP3 inflammasome activation was determined by western blot in THP-1 cells following exposure to 0.2 μg/ml LPS for 3 hours (Signal 1), followed by exposure to 10 μM nigericin for 30 min or for 2 hours (Signal 2). The panels **(a, b)** indicate western blot of **(a) CASP1** in the cellular protein extract, and **(b) IL-1β** in the culture supernatant.

Gene Chip Fluidic Station 450 (Affymetrix), and scanned by the Gene Chip Scanner 3000 7G (Affymetrix). The raw data were expressed as CEL files and normalized by the Robust Multi Array average (RMA) method with the Expression Console software (Affymetrix).

Quantitative reverse transcription (RT)-polymerase chain reaction (qPCR) analysis

DNase-treated total RNA isolated from THP-1 cells was processed for cDNA synthesis using oligo(dT)$_{12\text{-}18}$ primers and Super Script II reverse transcriptase (Invitrogen). Then, cDNA was amplified by PCR in Light Cycler ST300 (Roche Diagnostics, Tokyo, Japan) using SYBR Green I and a panel of sense and antisense primer sets following: 5'ccagcactgccaaactggactact3' and 5' acagctcagcaaagccagggatct3' for an 162 bp product of nuclear receptor subfamily 4, group A, member 1 (NR4A1); 5'ccaaagccgaccaagacctgcttt3' and 5'ctgtgcaagaccaccccattgcaa3' for an 124 bp product of nuclear receptor subfamily4, group A, member2 (NR4A2); 5'gagggctgcaagggctttttcaag3' and 5' gagggctgagaaggttcctgttgt3' for a 242 bp product of nuclear receptor subfamily 4, group A, member 3 (NR4A3); and 5'ccatgttcgtcatgggtgtgaacca3' and 5'gccagtagaggcagggatgatgttc3' for a 251 bp product of the glyceraldehyde-3-phosphate dehydrogenase (G3PDH) gene that serves as an endogenous control. The expression levels of target genes were standardized against the levels of G3PDH detected in the corresponding cDNA samples. All the assays were performed in triplicate.

Molecular network analysis

To identify biologically relevant molecular networks, we imported corresponding Entrez Gene IDs into Ingenuity Pathways Analysis (IPA) (Ingenuity Systems, Redwood City, CA, USA), KeyMolnet (Institute of Medicinal Molecular Design, Tokyo, Japan), or Search Tool for the Retrieval of Interacting Genes/Proteins (STRING) 9.1. STRING is an open-access database, while IPA and KeyMolnet are commercial resources.

STRING is a database that contains known and predicted, physiological and functional protein-protein interactions composed of 5,214,234 proteins from 1133 organisms [13]. STRING integrates the information from numerous resources, including experimental repositories, computational prediction methods, and public text collections. By uploading the list of UniProt IDs or Gene Symbols, STRING illustrates the union of all possible association networks.

IPA is a knowledgebase that contains approximately 3,000,000 biological and chemical interactions and functional annotations with definite scientific evidence. By uploading the list of Gene IDs and expression values, the network-generation algorithm identifies focused genes integrated in a global molecular network. IPA calculates the score p-value that reflects the statistical significance of association between the genes and the networks by the Fisher's exact test.

KeyMolnet contains knowledge-based contents on 164,000 relationships among human genes and proteins, small molecules, diseases, pathways and drugs [14]. They include the core contents collected from selected review articles with the highest reliability. By importing the list of Gene ID and expression values, KeyMolnet automatically provides corresponding molecules as nodes on the network. The neighboring network-search algorithm selected one or more molecules as starting points to generate the network of all kinds of molecular interactions around starting molecules, including direct activation/inactivation, transcriptional activation/repression, and the complex formation within one path from starting points. The generated network was compared side by side with 501 human canonical pathways of the KeyMolnet library. The algorithm counting the number of overlapping molecular relations between the extracted network and the canonical pathway makes it possible to identify the canonical pathway showing the most significant contribution to the

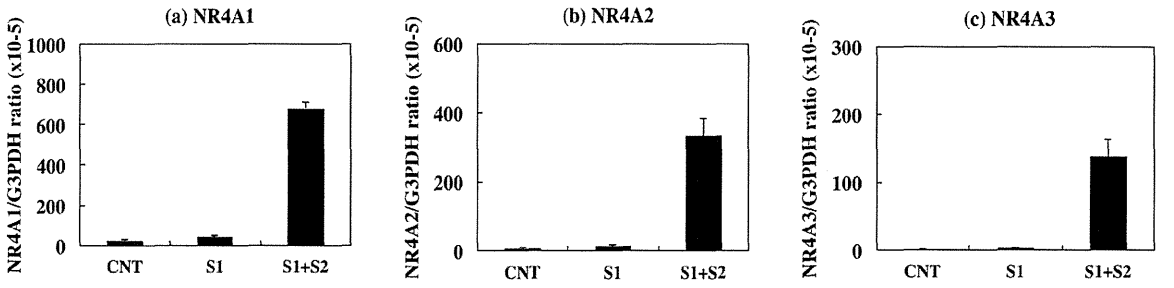

Figure 3: Upregulated expression of NR4A family members in THP-1 cells during NLRP3 inflammasome activation. The levels of expression of NR4A1, NR4A2, and NR4A3 transcripts in THP-1 cells following exposure to 0.2 μg/ml LPS for 3 hours (Signal 1; S1), followed by exposure to 10 μM nigericin for 2 hours (Signal 2; S2) were determined by qPCR. They were standardized against the levels of G3PDH detected in the corresponding cDNA samples. The panels **(a-c)** indicate qPCR of **(a) NR4A1**, **(b) NR4A2**, and **(c) NR4A3**. The bars represent **CNT** (LPS -, nigericin -), **S1** (LPS +, nigericin -), and **S1+S2** (LPS+, nigericin +).

extracted network.

Results

NLRP3 inflammasome activation in THP-1 cells following introduction of two-step signals

First, by western blot analysis, we studied NLRP3 inflammasome activation in THP-1 treated initially with exposure to 0.2 μg/ml LPS for 3 hours (Signal 1), followed by exposure to 10 μM nigericin for 30 min or 2 hours (Signal 2). The consecutive load of Signal 1 and Signal 2 markedly activated NLRP3 inflammasome in THP-1 cells, as indicated by production of cleaved products of CASP1 (Figure 2, panel a) and IL-1β (Figure 2, panel b). In contrast, the introduction of Signal 1 alone was not enough to activate NLRP3 inflammasome in THP-1 cells (Figure 2, panels a and b).

Gene expression profile during NLRP3 inflammasome activation

Next, we studied the genome-wide gene expression profile of THP-1 cells pretreated with 0.2 μg/ml LPS for 3 hours (Signal 1), washed by PBS, and exposed to 10 μM nigericin or vehicle for 2 hours (Signal 2). Then, total RNA was immediately processed for gene expression profiling on a Human Gene 1.0 ST Array. To identify NLRP3 inflammasome activation-responsive genes, we extracted the set of 83 annotated and protein-coding genes that satisfied fold change (FC) in Signal 1 (the presence of LPS versus the absence of LPS) smaller than 2-fold and FC in Signal 2 (the presence of nigericin versus the absence of nigericin) greater than 2-fold (Table 1). This gene enrichment procedure minimized the genes that were activated simply by exposure to LPS alone but not directly related to NLRP3 inflammasome activation.

Most notably, three members of NR4A nuclear receptor family, such as NR4A1 (NUR77), NR4A2 (NURR1), and NR4A3 (NOR1), were identified as those ranked within top 10 genes. Coordinated up regulation of NR4A1, NR4A2, and NR4A3 in NLRP3 inflammasome-activated THP-1 cells was validated by qPCR (Figure 3, panels a-c). Signal 1 alone mildly elevated expression of these mRNA levels, whereas introduction of Signal 2 after Signal 1 markedly elevated the levels of NR4A1, NR4A2, and NR4A3 transcripts with a 16-fold, 25-fold, or 51-fold increase, respectively. We also identified early growth response (EGR) family members, such as EGR1, EGR2, and EGR3, which belong to a family of zinc finger transcription factors involved in the regulation of cell growth, differentiation, and survival, NF-κB inhibitor (IκB) family members, such as NFKBIZ, NFKBID, and NFKBIA, along with a panel of pro inflammatory cytokines and chemokines, including CCL3, CCL3L3, IL8, CXCL2, CCL20, IL23A, and TNFSF9, as a subgroup of NLRP3 inflammasome activation-responsive genes.

Molecular network of NLRP3 inflammasome activation responsive genes

Next, by using three different bioinformatics tools for molecular network analysis based on knowledgebase, we studied biologically relevant molecular networks for the set of 83 NLRP3 inflammasome activation-responsive genes in THP-1 cells. The core analysis of IPA identified the networks defined as "Auditory and Vestibular System Development and Function, Embryonic Development, Organ Development" (p = 1.00E-32), "Cell Cycle, Cellular Development, Cell Death and Survival" (p = 1.00E-30) (Figure 4), and "Connective Tissue Disorders, Immunological Disease, Inflammatory Disease" (p = 1.00E-26) as top three most relevant functional networks. These results suggest that NLRP3 inflammasome activation-responsive genes play a pivotal role in cell development, death, and immune and inflammatory responses. KeyMolnet by the neighboring network-search algorithm operating on the core contents extracted the highly complex molecular network composed of 455 molecules and 529 molecular relations. The network showed the most statistically significant relationship with canonical pathways termed as "transcriptional regulation by AP-1" (p = 3.82E-184), "transcriptional regulation by NR4A" (p = 2.28E-105), and "transcriptional regulation by EGR" (p = 2.78E-99) (Figure 5). These results suggest a central role of transcription factors AP-1, NR4A, and EGR in regulation of expression of NLRP3 inflammasome activation-responsive genes, by acting as a hub of the molecular network.

Finally, STRING extracted a protein-protein interaction network, composed of 35 core molecules derived from the set of 83 NLRP3 inflammasome activation-responsive genes in THP-1 cells. In this network, both the set of NR4A family members NR4A1, NR4A2, and NR4A3 and EGR transcription factors EGR1, EGR2, and EGR3 constituted a close and intense protein interaction subnetwork (Figure 6).

Table 1: The set of 83 up-regulated genes in THP-1 monocytes following activation of NLRP3 inflammasome.

Rank	FC Related to Signal 1	FC Related to Signal 2	Entrez Gene ID	Gene Symbol	Gene Name
1	1.06819645	18.61247501	8013	NR4A3	nuclear receptor subfamily 4, group A, member 3
2	1.942378012	12.91651537	6348	CCL3	chemokine (C-C motif) ligand 3
3	1.63109973	11.69111	414062	CCL3L3	chemokine (C-C motif) ligand 3-like 3
4	1.100615838	11.24166642	9308	CD83	CD83 molecule
5	1.819566773	10.85127008	3576	IL8	interleukin 8
6	1.292541852	7.633454043	1960	EGR3	early growth response 3
7	0.948867136	6.576691539	4929	NR4A2	nuclear receptor subfamily 4, group A, member 2
8	1.116320272	5.51767318	3164	NR4A1	nuclear receptor subfamily 4, group A, member 1
9	1.842348508	5.271896351	64332	NFKBIZ	nuclear factor of kappa light polypeptide gene enhancer in B-cells inhibitor, zeta
10	1.268131184	4.992502002	643616	MOP-1	MOP-1
11	1.222058201	4.99018398	1959	EGR2	early growth response 2
12	1.716614387	4.456895103	5734	PTGER4	prostaglandin E receptor 4 (subtype EP4)
13	1.067764134	4.401932449	10746	MAP3K2	mitogen-activated protein kinase kinase kinase 2
14	1.076240121	4.353030131	2920	CXCL2	chemokine (C-X-C motif) ligand 2
15	1.443866138	4.329651804	6364	CCL20	chemokine (C-C motif) ligand 20
16	1.506881527	4.037790353	5743	PTGS2	prostaglandin-endoperoxide synthase 2 (prostaglandin G/H synthase and cyclooxygenase)
17	1.143021068	3.908082725	153020	RASGEF1B	RasGEF domain family, member 1B
18	1.00701348	3.793627448	1958	EGR1	early growth response 1
19	1.188818931	3.318906546	23645	PPP1R15A	protein phosphatase 1, regulatory (inhibitor) subunit 15A
20	0.978133301	3.154899408	65125	WNK1	WNK lysine deficient protein kinase 1
21	1.116953399	3.113268501	84807	NFKBID	nuclear factor of kappa light polypeptide gene enhancer in B-cells inhibitor, delta
22	1.431860551	3.025219884	51561	IL23A	interleukin 23, alpha subunit p19
23	0.654486344	2.985745104	645188	LOC645188	hypothetical LOC645188
24	1.082721348	2.867304268	1843	DUSP1	dual specificity phosphatase 1
25	1.877501415	2.813972064	8870	IER3	immediate early response 3
26	1.458901009	2.788511085	9021	SOCS3	suppressor of cytokine signaling 3
27	0.930381294	2.730662487	728715	LOC728715	ovostatin homolog 2-like
28	1.251031395	2.703465614	2353	FOS	v-fos FBJ murine osteosarcoma viral oncogene homolog
29	1.994627015	2.654181457	27289	RND1	Rho family GTPase 1
30	0.877732964	2.64583117	23499	MACF1	microtubule-actin crosslinking factor 1
31	1.18363314	2.591793912	7538	ZFP36	zinc finger protein 36, C3H type, homolog (mouse)
32	0.768263434	2.584281103	79101	TAF1D	TATA box binding protein (TBP)-associated factor, RNA polymerase I, D, 41kDa
33	1.895682029	2.568793654	90668	LRRC16B	leucine rich repeat containing 16B
34	0.916615124	2.536018037	259296	TAS2R50	taste receptor, type 2, member 50
35	0.895110685	2.535538194	728741	LOC728741	hypothetical LOC728741
36	0.870604266	2.532650507	84319	CMSS1	cms1 ribosomal small subunit homolog (yeast)
37	0.474895831	2.525788794	4072	EPCAM	epithelial cell adhesion molecule
38	1.667878267	2.514873802	1326	MAP3K8	mitogen-activated protein kinase kinase kinase 8
39	1.107775084	2.496005315	8744	TNFSF9	tumor necrosis factor (ligand) superfamily, member 9
40	1.024389944	2.491488658	4616	GADD45B	growth arrest and DNA-damage-inducible, beta
41	0.97810347	2.470592388	2354	FOSB	FBJ murine osteosarcoma viral oncogene homolog B
42	1.017380957	2.461870724	643036	SLED1	RTFV9368
43	1.017380957	2.377675786	2152	F3	coagulation factor III (thromboplastin, tissue factor)

44	1.038770533	2.373054125	1973	EIF4A1	eukaryotic translation initiation factor 4A, isoform 1
45	1.596962012	2.3683134	4792	NFKBIA	nuclear factor of kappa light polypeptide gene enhancer in B-cells inhibitor, alpha
46	0.872659044	2.354224669	1736	DKC1	dyskeratosis congenita 1, dyskerin
47	1.254570022	2.347010028	50515	CHST11	carbohydrate (chondroitin 4) sulfotransferase 11
48	0.818985035	2.34454831	50840	TAS2R14	taste receptor, type 2, member 14
49	0.649089802	2.278082518	85028	SNHG12	small nucleolar RNA host gene 12 (non-protein coding)
50	0.978928228	2.273044623	2889	RAPGEF1	Rap guanine nucleotide exchange factor (GEF) 1
51	0.689249392	2.247537218	55795	PCID2	PCI domain containing 2
52	0.827575589	2.246739728	54765	TRIM44	tripartite motif-containing 44
53	1.067300921	2.243145194	1263	PLK3	polo-like kinase 3 (Drosophila)
54	0.767788042	2.229552244	337867	UBAC2	UBA domain containing 2
55	1.306111439	2.229215371	3759	KCNJ2	potassium inwardly-rectifying channel, subfamily J, member 2
56	1.925222241	2.191743556	80149	ZC3H12A	zinc finger CCCH-type containing 12A
57	0.882964289	2.185060168	58155	PTBP2	polypyrimidine tract binding protein 2
58	1.545906426	2.181251323	56895	AGPAT4	1-acylglycerol-3-phosphate O-acyltransferase 4 (lysophosphatidic acid acyltransferase, delta)
59	1.05509141	2.155321381	10896	OCLM	oculomedin
60	1.05361515	2.15489714	9659	PDE4DIP	phosphodiesterase 4D interacting protein
61	0.986553364	2.153150265	3047	HBG1	hemoglobin, gamma A
62	0.87493697	2.150450624	100507607	NPIPB9	nuclear pore complex interacting protein family, member B9
63	1.201327908	2.147514699	259292	TAS2R46	taste receptor, type 2, member 46
64	0.885483295	2.144478729	51574	LARP7	La ribonucleoprotein domain family, member 7
65	0.970156229	2.132807866	9839	ZEB2	zinc finger E-box binding homeobox 2
66	0.700126731	2.102345827	100133941	CD24	CD24 molecule
67	1.471640204	2.097753274	6303	SAT1	spermidine/spermine N1-acetyltransferase 1
68	0.796744464	2.080051151	9572	NR1D1	nuclear receptor subfamily 1, group D, member 1
69	1.754590053	2.069409283	10129	FRY	furry homolog (Drosophila)
70	1.117049405	2.06451372	5586	PKN2	protein kinase N2
71	1.084905208	2.058951728	339883	C3orf35	chromosome 3 open reading frame 35
72	1.007649566	2.047104863	1195	CLK1	CDC-like kinase 1
73	1.001286612	2.046307571	1185	CLCN6	chloride channel 6
74	1.005938423	2.043756057	338442	HCAR2	hydroxycarboxylic acid receptor 2
75	0.88066058	2.04297423	6144	RPL21	ribosomal protein L21
76	1.048011825	2.039547357	1844	DUSP2	dual specificity phosphatase 2
77	1.361895488	2.039480914	3092	HIP1	huntingtin interacting protein 1
78	0.951119813	2.038925421	388022	LOC388022	hypothetical gene supported by AK131040
79	0.888482949	2.018363478	144132	DNHD1	dynein heavy chain domain 1
80	0.972189862	2.012125102	23049	SMG1	SMG1 homolog, phosphatidylinositol 3-kinase-related kinase (C. elegans)
81	0.89112764	2.007348359	6181	RPLP2	ribosomal protein, large, P2
82	0.798221473	2.005195646	23329	TBC1D30	TBC1 domain family, member 30
83	1.206469961	2.003702064	3726	JUNB	jun B proto-oncogene

To activate NLRP3 inflammasome, THP-1 cells were initially exposed to 0.2 μg/ml LPS for 3 hours (Signal 1). They were then washed by PBS and exposed to 10 μM nigericin for 2 hours (Signal 2 after Signal 1). At 5 hours after initiation of the treatment, total RNA was isolated and processed for gene expression profilong on a Human Gene 1.0 ST Array. The set of 83 genes that satisfy fold change (FC) related to Signal 1 (LPS + versus LPS -) smaller than 2-fold and FC related to Signal 2 (nigericin + versus nigericin -) greater than 2-fold are shown with FC, Entrez Gene ID, Gene Symbol, and Gene Name.

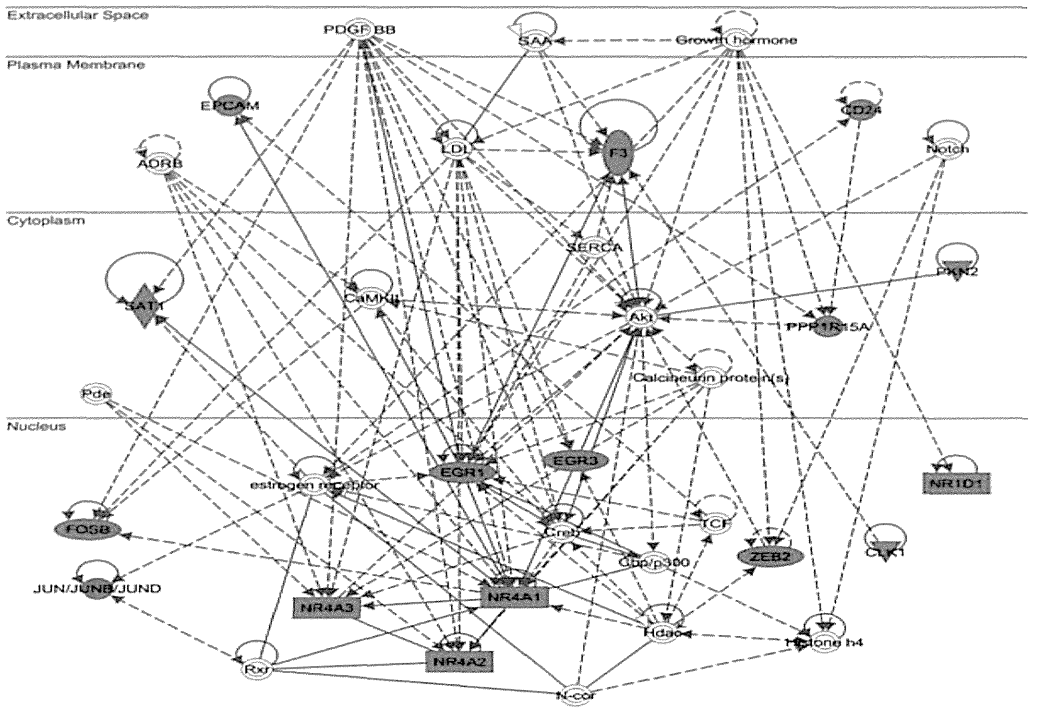

Figure 4: IPA molecular network of NLRP3 inflammasome activation-responsive genes. Entrez Gene IDs corresponding to the set of 83 NLRP3 inflammasome activation-responsive genes in THP-1 cells (Table 1) were imported into the core analysis tool of IPA. The functional network defined as "Cell Cycle, Cellular Development, Cell Death and Survival" is shown. Red nodes indicate NLRP3 inflammasome activation-responsive genes.

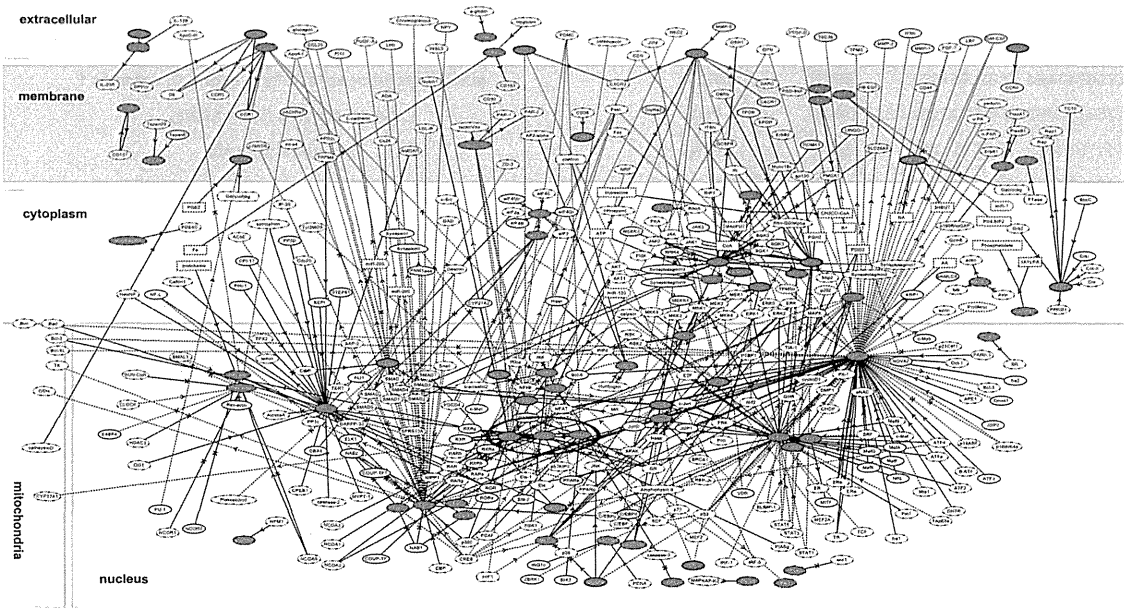

Figure 5: KeyMolnet molecular network of NLRP3 inflammasome activation-responsive genes. Entrez Gene IDs corresponding to the set of 83 NLRP3 inflammasome activation-responsive genes in THP-1 cells (Table 1) were imported into KeyMolnet. The neighboring network-search algorithm operating on the core contents extracted the highly complex molecular network. Red nodes represent NLRP3 inflammasome activation-responsive genes, while white nodes exhibit additional nodes extracted automatically from the core contents of KeyMolnet to establish molecular connections. The molecular relation is indicated by solid line with arrow (direct binding or activation), solid line with arrow and stop (direct inactivation), solid line without arrow (complex formation), dash line with arrow (transcriptional activation), and dash line with arrow and stop (transcriptional repression). The cluster of NR4A1, NR4A2, and NR4A3 is highlighted by blue circle.

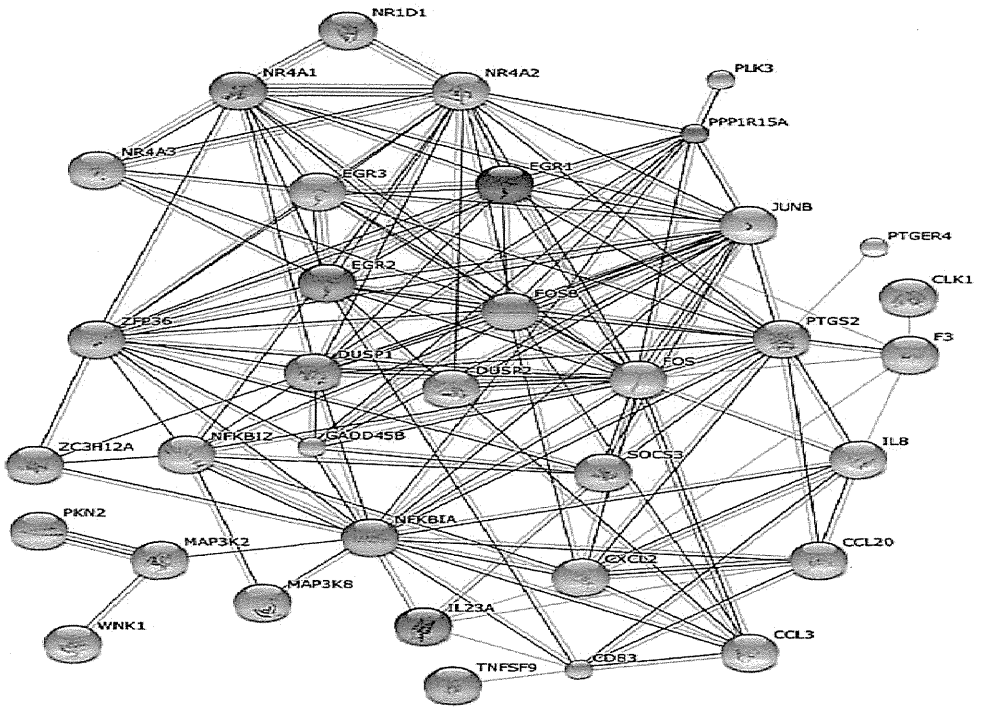

Fig. 6. STRING molecular network of NLRP3 inflammasome activation-responsive genes. Gene Symbols corresponding to the set of 83 NLRP3 inflammasome activation-responsive genes in THP-1 cells (Table 1) were imported into STRING. The set of 35 molecules constructing the protein-protein interaction network are shown on the evidence view of STRING.

Discussion

By genome-wide gene expression profiling, we identified the set of 83 NLRP3 inflammasome activation-responsive genes in THP-1 cells sequentially given two-step signals. Among them, we found three members of NR4A nuclear receptor family, such as NR4A1, NR4A2, and NR4A3, three members of EGR family, such as EGR1, EGR2, and EGR3, three members of IκB family, such as NFKBIZ, NFKBID, and NFKBIA as a noticeable subset of NLRP3 inflammasome activation-responsive genes. By molecular network analysis, we found that they play a central role in cellular development and death, and immune and inflammatory responses, where transcription factors AP-1, NR4A, and EGR serve as a hub in the molecular network. Because THP-1 is a spontaneously immortalized human monocytic cell line derived from an acute monocytic leukemia patient, the possibility could not be excluded that the molecular network we identified does not represent the physiological network of non-malignant human monocytes.

NR4A1, NR4A2, and NR4A3 are three closely related, highly homologous nuclear transcription factors of the steroid/thyroid hormone receptor superfamily, categorized as orphan nuclear receptors because of lack of their cognate ligands [15]. They are encoded by immediate early genes, rapidly induced by exposure of the cells to the serum, growth factors, cytokines, and peptide hormones. NR4A receptors act as a transcription factor for a battery of downstream genes involved in cell proliferation, apoptosis, DNA repair, inflammation, and angiogenesis [16]. Accumulating evidence indicates that NR4A family exerts not only proinflammatory but also anti-inflammatory effects on various cell types. NR4A receptors play a pivotal role in development of regulatory T (Treg) cells in the thymus [17]. Knockdown of either NR4A1 or NR4A3 elevates the levels of production of IL-1β, IL-8, and MCP-1 in THP-1 cells [18]. By binding directly to NF-κB p65, a central regulator of innate and adaptive immune response, NR4A1 recruits the CoREST corepressor complex on gene promoter and inhibits transcription of proinflammatory genes in mouse microglia and astrocytes [19]. Adenosine monophosphate released from apoptotic cells, when metabolized to adenosine, activates macrophages to express NR4A1, NR4A2, and NR4A3 that play a role in suppression of inflammation during engulfment of apoptotic cells [20]. Recently, we found that NR4A2 is one of vitamin D receptor-target genes with protective function against development of MS by analyzing a chromatin immunoprecipitation followed by deep sequencing (ChIP-Seq) dataset derived from immortalized B cells and THP-1 cells [21]. All of these observations suggest that NR4A proteins, whose expression is induced by proinflammatory mediators, serve as a safety valve for shutting down sustained inflammation that is amplified by NLRP3 inflammasome activation. Consistent with this view, IκB family members acting as a negative regulator of NF-κB activation, such as NFKBIZ, NFKBID, and NFKBIA [22-24], are coordinately induced along with enhanced expression of NR4A family, suggesting that these molecules constitute a negative feedback loop for NLRP3 inflammasome activation.

EGR family constitutes a family of zinc finger transcription factors very rapidly and transiently induced in various cell types without *de novo* protein synthesis following exposure to mitogenic signals [25,26]. EGR1 functions as a positive regulator for T and B cell functions, by regulating transcription of the genes encoding key cytokines and costimulatory molecules, while EGR2 and EGR3 act as a negative regulator essential for induction of anergy [27]. EGR1 downregulates the expression of itself by binding to an EGR1-binding site located on its own promoter [28]. Furthermore, EGR1 directly activates transcription of NR4A1 (nur77) in mouse IgM^+ B cells [29]. Deletion of EGR2 and EGR3 in mouse T and B cells causes a lethal autoimmune syndrome characterized by excessive production of proinflammatory cytokines accompanied by overactivation of STAT1 and STAT3 [30]. Importantly, we identified SOCS3, a potent inhibitor of STAT3 activation [31], as one of NLRP3 inflammasome activation-responsive genes (Rank 26 in Table 1). These observations suggest the working hypothesis that the EGR family members are actively involved in resolution of sustained inflammation amplified by NLRP3 inflammasome activation.

Conclusion

By genome-wide gene expression profiling, we identified the set of 83 NLRP3 inflammasome activation-responsive genes in THP-1 cells. Among them, we found NR4A nuclear receptor family, EGR family, and IκB family as a group of the genes that possibly constitute a negative feedback loop for shutting down sustained inflammation following NLRP3 inflammasome activation. By molecular network analysis, we found that NLRP3 inflammasome activation-responsive genes play a pivotal role in cellular development and death, and immune and inflammatory responses, where transcription factors AP-1, NR4A, and EGR act as a hub in the molecular network.

Acknowledgement

This work was supported by the JSPS KAKENHI (C25430054), and the Intractable Disease Research Center (IDRC) project, the Ministry of Education, Culture, Sports, Science and Technology (MEXT), Japan, and the grant from the National Center for Geriatrics and Gerontology (NCGC 26-20). The authors would thank Ms. Aki Takaoka for her invaluable help in microarray analysis. The microarray data are available from the Gene Expression Omnibus (GEO) under the accession number GSE58959.

References

1. Schroder K, Tschopp J. The inflammasomes. Cell. 2010; 140: 821-832.
2. Menu P, Vince JE. The NLRP3 inflammasome in health and disease: the good, the bad and the ugly. Clin Exp Immunol. 2011; 166: 1-15.
3. Wang H, Mao L, Meng G. The NLRP3 inflammasome activation in human or mouse cells, sensitivity causes puzzle. Protein Cell. 2013; 4: 565-568.
4. Walsh JG, Muruve DA, Power C. Inflammasomes in the CNS. Nat Rev Neurosci. 2014; 15: 84-97.
5. Zhou R, Yazdi AS, Menu P, Tschopp J. A role for mitochondria in NLRP3 inflammasome activation. Nature. 2011; 469: 221-225.
6. Shimada K, Crother TR, Karlin J, Dagvadorj J, Chiba N, Chen S, et al. Oxidized mitochondrial DNA activates the NLRP3 inflammasome during apoptosis. Immunity. 2012; 36: 401-414.
7. Di Virgilio F. Liaisons dangereuses: P2X(7) and the inflammasome. Trends Pharmacol Sci. 2007; 28: 465-472.
8. Halle A, Hornung V, Petzold GC, Stewart CR, Monks BG, Reinheckel T, et al. The NALP3 inflammasome is involved in the innate immune response to amyloid-beta. Nat Immunol. 2008; 9: 857-865.
9. Jourdan T, Godlewski G, Cinar R, Bertola A, Szanda G, Liu J, et al. Activation of the Nlrp3 inflammasome in infiltrating macrophages by endocannabinoids mediates beta cell loss in type 2 diabetes. Nat Med. 2013; 19: 1132-1140.
10. Heneka MT, Kummer MP, Stutz A, Delekate A, Schwartz S, Vieira-Saecker A, Griep A. NLRP3 is activated in Alzheimer's disease and contributes to pathology in APP/PS1 mice. Nature. 2013; 493: 674-678.
11. Kawana N, Yamamoto Y, Ishida T, Saito Y, Konno H, Arima K, et al. Reactive *astrocytes and perivascular macrophages express* NLRP3 *inflammasome* in active demyelinating lesions of multiple sclerosis and necrotic lesions of neuromyelitis optica and cerebral infarction. Clin Exp Neuroimmunol. 2013; 4: 296-304.
12. Gris D, Ye Z, Iocca HA, Wen H, Craven RR, Gris P, Huang M. NLRP3 plays a critical role in the development of experimental autoimmune encephalomyelitis by mediating Th1 and Th17 responses. J Immunol. 2010; 185: 974-981.
13. Franceschini A, Szklarczyk D, Frankild S, Kuhn M, Simonovic M, Roth A, Lin J. STRING v9.1: protein-protein interaction networks, with increased coverage and integration. Nucleic Acids Res. 2013; 41: D808-815.
14. Satoh J. Bioinformatics approach to identifying molecular biomarkers and networks in multiple sclerosis. Clin Exp Neuroimmunol. 2010; 1: 127–140.
15. Zhao Y, Bruemmer D. NR4A orphan nuclear receptors: transcriptional regulators of gene expression in metabolism and vascular biology. Arterioscler Thromb Vasc Biol. 2010; 30: 1535-1541.
16. Mohan HM, Aherne CM, Rogers AC, Baird AW, Winter DC, Murphy EP. Molecular pathways: the role of NR4A orphan nuclear receptors in cancer. Clin Cancer Res. 2012; 18: 3223-3228.
17. Sekiya T, Kashiwagi I, Yoshida R, Fukaya T, Morita R, Kimura A, Ichinose H. Nr4a receptors are essential for thymic regulatory T cell development and immune homeostasis. Nat Immunol. 2013; 14: 230-237.
18. Bonta PI, van Tiel CM, Vos M, Pols TW, van Thienen JV, Ferreira V, et al. Nuclear receptors Nur77, Nurr, and NOR-1 expressed in atherosclerotic lesion macrophages reduce lipid loading and inflammatory responses. Arterioscler Thromb Vasc Biol. 2006; 26: 2288-2294.
19. Saijo K, Winner B, Carson CT, Collier JG, Boyer L, Rosenfeld MG, et al. A Nurr1/CoREST pathway in microglia and astrocytes protects dopaminergic neurons from inflammation-induced death. Cell. 2009; 137: 47-59.
20. Yamaguchi H, Maruyama T, Urade Y, Nagata S. Immunosuppression via adenosine receptor activation by adenosine monophosphate released from apoptotic cells. Elife. 2014; 3: e02172.
21. Satoh J, Tabunoki H. Molecular network of chromatin immunoprecipitation followed by deep sequencing-based vitamin D receptor target genes. Mult Scler. 2013; 19: 1035-1045.
22. Muta T, Yamazaki S, Eto A, Motoyama M, Takeshige K. IkappaB-zeta, a new anti-inflammatory nuclear protein induced by lipopolysaccharide, is a negative regulator for nuclear factor-kappaB. J Endotoxin Res. 2003; 9: 187-191.
23. Tergaonkar V, Correa RG, Ikawa M, Verma IM. Distinct roles of IkappaB proteins in regulating constitutive NF-kappaB activity. Nat Cell Biol. 2005; 7: 921-923.
24. Kuwata H, Matsumoto M, Atarashi K, Morishita H, Hirotani T, Koga R, et al. IkappaBNS inhibits induction of a subset of Toll-like receptor-dependent genes and limits inflammation. Immunity. 2006; 24: 41-51.
25. Christy B, Nathans D. DNA binding site of the growth factor-inducible protein Zif268. Proc Natl Acad Sci U S A. 1989; 86: 8737-8741.
26. Beckmann AM, Wilce PA. Egr transcription factors in the nervous system. Neurochem Int. 1997; 31: 477-510.
27. Gómez-Martín D, Díaz-Zamudio M, Galindo-Campos M, Alcocer-Varela J. Early growth response transcription factors and the modulation of immune

response: implications towards autoimmunity. Autoimmun Rev. 2010; 9: 454-458.

28. Cao X, Mahendran R, Guy GR, Tan YH. Detection and characterization of cellular EGR-1 binding to its recognition site. J Biol Chem. 1993; 268: 16949-16957.

29. Dinkel A, Warnatz K, Ledermann B, Rolink A, Zipfel PF, Bürki K, et al. The transcription factor early growth response 1 (Egr-1) advances differentiation of pre-B and immature B cells. J Exp Med. 1998; 188: 2215-2224.

30. Li S, Miao T, Sebastian M, Bhullar P, Ghaffari E, Liu M, et al. The transcription factors Egr2 and Egr3 are essential for the control of inflammation and antigen-induced proliferation of B and T cells. Immunity. 2012; 37: 685-696.

31. Carow B, Rottenberg ME. SOCS3, a Major Regulator of Infection and Inflammation. Front Immunol. 2014; 5: 58.

Citation: Kawana N, Yamamoto Y, Kino Y and Jun-ichi Satoh. Molecular Network of NLRP3 Inflammasome Activation-Responsive Genes in a Human Monocyte Cell Line. Austin J Clin Immunol. 2014;1(4): 10.

Clinical Investigative Study

Usefulness of SWI for the Detection of Iron in the Motor Cortex in Amyotrophic Lateral Sclerosis

Yuko Adachi, MD, PhD, Noriko Sato, MD, PhD, Yuko Saito, MD, PhD, Yukio Kimura, MD, Yasuhiro Nakata, MD, PhD, Kimiteru Ito, MD, PhD, Kouhei Kamiya, MD, PhD, Hiroshi Matsuda, MD, PhD, Tadashi Tsukamoto, MD, PhD, Masahumi Ogawa, MD, PhD

From the National Center Hospital of Neurology and Psychiatry Radiology, Kodaira, Tokyo, Japan

ABSTRACT

PURPOSE

The purpose of the present retrospective study was to evaluate the sensitivity of susceptibility-weighted imaging (SWI) compared to conventional spin-echo T2-weighted and T2*-weighted images in detecting iron deposition in the motor cortex of amyotrophic lateral sclerosis (ALS) patients in comparison with age-matched normal controls. We also investigated the etiology of the low signal referring to the pathology of one autopsy case.

METHODS

This retrospective magnetic resonance (MR) study included 23 ALS patients and 28 age-matched normal controls. The signal intensity of the motor cortex was scored by SWI, conventional T2-weighted images and T2*-weighted images. A postmortem study of one patient was also performed.

RESULTS

On SWI, there was a significant difference between the precentral cortical signal intensity scores in the ALS patients and the controls ($P < .0001$). The total scores of signal intensities of the precentral cortex were positively correlated with age in the normal controls ($r = .494$), but no correlation was observed in the ALS patients. The postmortem study showed intensely stained microglias and macrophages after antiferritin antibody staining in the precentral cortices.

CONCLUSIONS

Decreased signal intensity of the motor cortex on SWI may serve a useful role in ALS diagnoses, particularly in young patients. MR images were also helpful for speculating on the etiology of ALS.

Keywords: validation, erectile dysfunction, prostate cancer, alprostadil.

Acceptance: Received August 2, 2013, and in revised form January 7, 2014. Accepted for publication March 2, 2014.

Correspondence: Address correspondence to Noriko Sato, National Center Hospital of Neurology and Psychiatry Radiology, 4-1-1 Ogawahigashi-chyo Kodaira, Tokyo 187-8551, Japan. E-mail: snoriko@ncnp.go.jp.

Conflicts of Interest: *The authors report no conflicts of interest.*

J Neuroimaging 2014;00:1-9.
DOI: 10.1111/jon.12127

Introduction

Amyotrophic lateral sclerosis (ALS) is a degenerative disorder characterized by the loss of both upper and lower motor neurons. The diagnosis of ALS is based on clinical presentation, course, and neurological findings[1,2] diagnosis of late-stage ALS is not difficult but that of early-phase ALS is more problematic. In particular, lower motor neuron (LMN) dysfunction can be confirmed by electromyogram (EMG) and muscle biopsy, whereas upper motor neuron (UMN) involvement is more difficult to detect.[1,2]

Several reports providing the radiological findings of ALS patients have been published. The presence of low signal intensity in the motor cortex and high signal intensity in the pyramidal tract on T2-weighted images and the presence of atrophy of the motor cortex were observed by conventional magnetic resonance (MR) techniques.[3,4] However, these findings are nonspecific in older patients and are commonly absent in the early phases of the disease. Reports involving non conventional MR techniques, including MR spectroscopy, magnetization transfer imaging, functional MR imaging and diffusion tensor imaging are accumulating in patients with motor neuron diseases.[4–15] Although the diagnostic values in the clinical assessment of ALS are uncertain and remain to be established, MR images have the potential to be used as diagnostic markers and are continuously improving as a modality for pursuing early diagnosis of ALS and evaluation of disease progression.

MR imaging is currently the best imaging technique for the in vivo detection of cerebral iron. Particularly, T2*-weighted gradient echo imaging was advocated as the most sensitive sequence for assessing hemosiderin depositions before susceptibility-weighted imaging (SWI) was developed.[16–18] SWI is a neuroimaging technique that uses tissue magnetic susceptibility differences to generate a unique contrast, different from that of spin density, T1-weighted, T2-weighted, and T2*-weighted imaging.[19] SWI offers information about any tissue or substances that has a different susceptibility in contrast

with its surrounding structures such as deoxygenated blood, hemosiderin, ferritin or calcium. Preliminary studies suggested that SWI is more sensitive than T2*-weighted imaging for detecting brain iron.[20,21] These studies concluded that SWI methods provide significantly higher-contrast images of lesions such as cavernous hemangiomas, cerebral microbleeds, and brain tumors.

There are numerous neurologic disorders or conditions for which the use of methods that detect iron depositions in the brain can be beneficial. These conditions include aging, multiple sclerosis, stroke, trauma, vascular malformation, tumors, and neurodegenerative diseases. Hemosiderin-containing areas in the brain tissue demonstrate more prominent hypointensity on T2*-weighted images than on conventional spin echo T2-weighted images (In the present study, conventional spin-echo T2-weighted images are defined as single-echo to distinguish them from fast spin-echo sequences). However, it was recently determined that ferritin showed more prominent image contrast on conventional spin-echo T2-weighted images than on T2*-weighted images.[22]

The purpose of the present retrospective study was to evaluate the sensitivity of SWI compared to conventional spin-echo T2-weighted and T2*-weighted images in detecting iron deposition in the motor cortex of ALS patients in comparison with age-matched normal controls. A postmortem study using Berlin blue staining and antiferritin antibody staining was also conducted for one of the ALS patients.

Materials and Methods

Subjects

A list of the MR imaging studies of patients suspected with ALS was acquired from a searching the radiology information system of our institution (National Center Hospital of Neurology and Psychiatry) between January 2007 and December 2009. The diagnoses of ALS were made by neurologists who each had more than 10 years of experience in the diagnosis of neurological degenerative diseases. A total of 23 patients diagnosed with from definite ALS to possible ALS were identified. We retrospectively reviewed all of the patients' brain MR images. The gender and age at the time of imaging were as follows: 13 males and 10 females, ranging in age from 44 to 77 years old, mean age 63.0 ± 10.4 years old. The diagnosis of ALS was made by applying the El Escorial revised criteria[23] to the findings of clinical and EMG examinations. The breakdown was as follows: six definite ALS, seven probable ALS, five clinically probable laboratory-supported ALS, and five possible ALS. Patients with brain damage from an ischemic event or from another demyelination disease such as, cervical spondylosis or myasthenia gravis were excluded from this series. The time between the onset of symptoms and the MR study ranged from 6 months to 6 years (average, 27.9 months). Cerebral abnormalities including cerebrovascular diseases were not seen in any MR examinations. The postmortem brain of one patient with ALS was studied by means of Berlin blue and antiferritin antibody staining. Twenty-eight age-matched normal controls (13 males and 15 females, ranging in age from 33 to 82 years old, mean 63.2 ± 13.7 years), were also examined by MR imaging as controls. Institutional review board approval was obtained and written informed consent was obtained from the control subjects. Our local ethics committee did not require patient informed consent for the retrospective review.

Images and Data Analysis

MR examinations were performed with a 1.5-T imager (Symphony, Siemens, Erlangen, Germany) with a 12-channel head coil. The standard protocol included axial conventional spin-echo T2-weighted imaging (TR/TE, 3200/90 ms; flip angle, 90°; FOV, 230 mm; matrix, 256 × 153.6; section thickness, 5 mm; intersection gap, 1.75 mm; acquisition time, 5.8 minutes) and T2*-weighted imaging (TR/TE, 733/25 ms; flip angle, 20°; FOV, 230 × 207 mm; matrix, 320 × 240; section thickness, 5 mm; intersection gap, 1.75 mm; acquisition time, 4.4 minutes). Three-dimensional SWI was acquired with the following parameters: TR/TE, 47/40 ms; flip angle, 15°; FOV, 230 × 172.5 mm; matrix, 320 × 294; section thickness, 1.8 mm; acquisition time, 7.4 minutes. After the data were acquired, there was additional postprocessing that accentuated the signal intensity loss caused by any susceptibility effects. The sequence, along with its automatic postprocessing, is currently available for Siemens 1.5 MR imaging scanner platforms. SWI reconstructed with a minimum intensity projection (minIP) technique (10.4-mm thickness and 1.3-mm gap) was taken on for our review.

All 23 patients underwent SWI studies. Conventional spin-echo T2-weighted images were not acquired in 3 patients, and T2*-weighted images were not obtained in 2 patients. All controls underwent SWI, conventional spin-echo T2-weighted imaging, and T2*-weighted imaging.

The SWI were evaluated with regular clinical window width (400 ± 100) and level (200 ± 100) settings. Imaging assessment in the patients and controls was based on agreement between two neuroradiologists who reviewed the images (Y.A. and N.S., with 10 and 21 years of experience with MR images, respectively). Each neuroradiologist made initial evaluations independently, and any disagreements regarding the final conclusion were resolved by consensus. Each observer was blinded to the other observer's scores, the clinical information, and the condition of the subject (patient or control).

To identify the central sulcus or motor cortex on MR images, we used the method of Iwasaki et al.[24] We used two transverse images on each sequence to evaluate the signal intensity of the motor cortex; the superior image was at the level of the semioval center, and the inferior image was at the level of the top slice of the lateral ventricle. The signal intensity of the motor cortex was compared with that of the superior frontal cortex and graded with a three-point scoring system as follows: isointense (score 0), mildly hypointense (score 1) or markedly hypointense (score 2) (Fig 1). In the statistical analysis, we used the total score of the superior and inferior images. If there was laterality of the signal intensity in the motor cortices, the higher scores were selected.

The statistical analysis was carried out using the χ^2 test to look for significant differences in signal intensity scores between the ALS patients and the normal controls. *P*-values below .01 were considered significant. We also evaluated the relationships between disease duration and imaging scores on SWI, using the Spearman correlation coefficient. The correlation between the signal intensity scores and age in the patients and normal

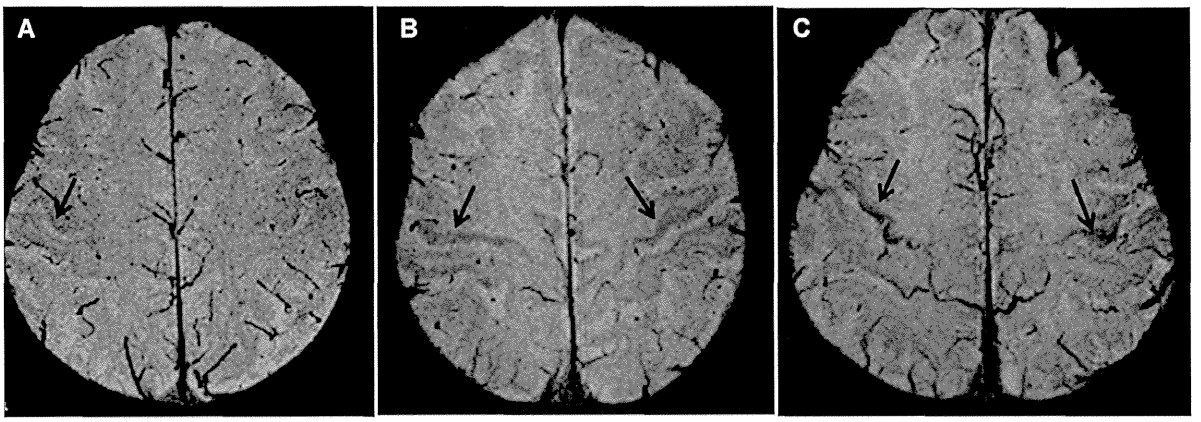

Fig 1. Three-point scoring system by visual assessment on minIp SWI. (A) Axial SWI of a superior slice shows that the right precentral cortex is as isointense as the superior frontal cortex (Score 0). (B) Mildly low signal intensity in both precentral cortices compared to the superior frontal cortex (Score 1). (C) Markedly low signal intensity in bilateral precentral cortices compared to the superior frontal cortex (Score 2).

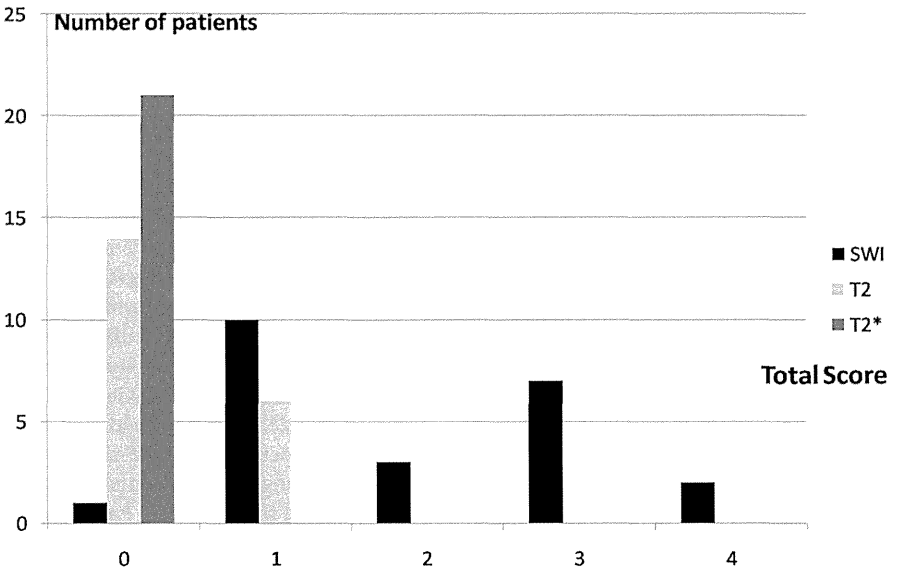

Fig 2. Total motor cortex scores of three sequences: SWI, conventional SE T2 and T2*-weighted images in ALS patients. SWI was the most sensitive sequence for detecting the low signal intensity of the precentral cortex in the ALS patients compared to the other two sequences.

controls were assessed by computing the Spearman correlation coefficient. We also made charts of the relationship between the certainty in ALS diagnosis criteria and the signal intensity score on both SWI and conventional T2-weighted imaging; no statistical analysis was done for these categories because of the small numbers of patients in each.

Neuropathology

Among the 23 ALS cases, a postmortem study was permitted in one case. Neuropathological examination was performed in this case as well as in 10 age-matched control cases, following the reported Brain Bank for Aging Research protocol (www.mci.gr.jp/BrainBank/).[25] Briefly, six-μm-thick serial sections of formalin-fixed, paraffin-embedded representative areas were stained with hematoxylin and eosin and by the Klüver–Barrera method. In addition to routine staining, selected sections including the motor area were stained with Berlin blue stain. Immunohistochemical antibody staining using antiglial fibrillary acidic protein (polyclonal, Dako, Glostrup, Denmark), anti-CD68 (monoclonal, Dako), and antiferritin (polyclonal, monoclonal, Dako) was performed using a Ventana Discovery autoimmunostainer (Ventana, Tucson, AZ).

Results

MR Imaging Findings

The results of the total scores for each sequence in the ALS patients are summarized in Figure 2. SWI was the most sensitive sequence to detect low signal of motor cortex and T2*-weighted images was less sensitive than conventional

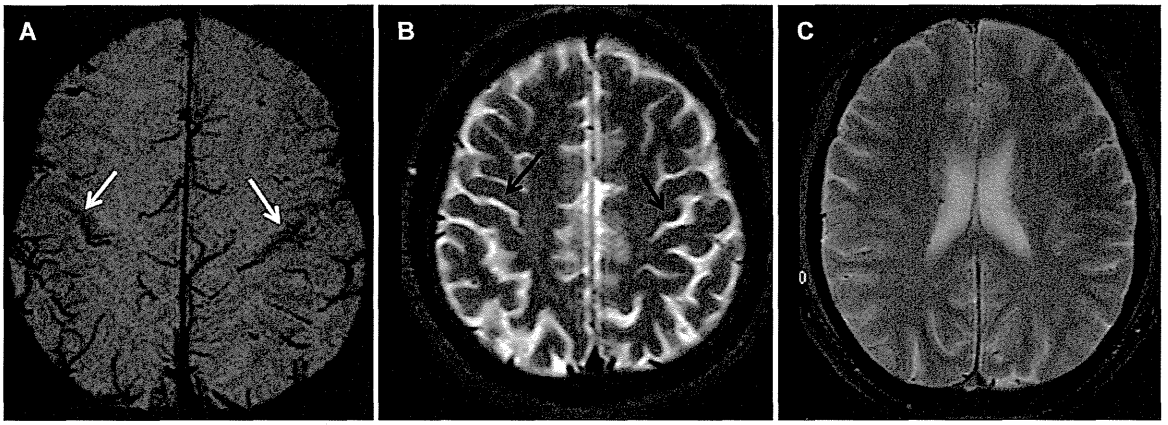

Fig 3. (A) Axial SWI (minIp) of a superior slice shows markedly low signal intensity in bilateral precentral cortices compared to the superior frontal cortices (Score 2). (B) Axial conventional T2-weighted image of a superior slice shows mildly low intensity in bilateral precentral cortices compared to the superior frontal cortices of the same slice (Score 1). (C) Axial T2*-weighted image of superior slice appears isointense compared to superior frontal cortices (Score 0).

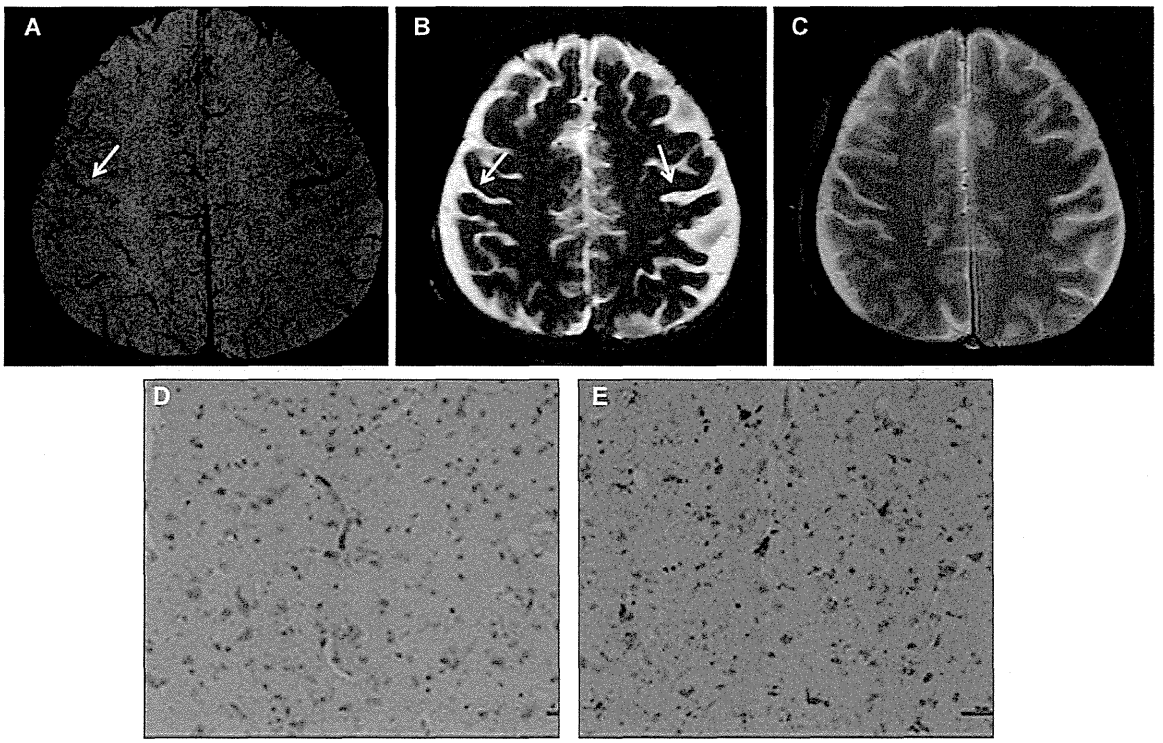

Fig 4. (A)The axial SWI (minIp) of superior slice appears markedly hypointense on the left side (black arrow) of the precentral cortex (Score 2) and moderately hypointense on the right side (white arrow) compared to the superior frontal cortex (Score 1). (B) Axial conventional T2-weighted image of the superior slice appears moderately hypointense in bilateral precentral cortices compared to the superior frontal gyrus of the same slice (Score 1). (C) Axial T2*-weighted image of superior slice appears isointense in bilateral precentral cortices compared to the superior-frontal cortex (total score 0). (D) Antiferritin antibody staining of the right motor cortex shows intensely stained microglias and macrophages. (E) Antiferritin antibody staining of the left motor cortex shows stronger stained microglias and macrophages than right side.

spin-echo T2-weighted images (Figs 3 and 4). The mean value of the total score on SWI in the ALS patients was 1.96 ± 1.15. SWI was only sequence getting total score of 4 as shown in Figure 2. All T2*-weighted images showed score 0. Of the group of normal controls, three of the 28 controls were assessed as a total score of 2, 10 had a total score of 1, and the remaining 15 had a total score of 0 on SWI (mean value: .57 ± .69). On spin-echo T2-weighted images, three controls were assessed with a total score of 1, and 25 controls were assessed as a score of 0. All controls had a score of 0 on T2*-weighted images.

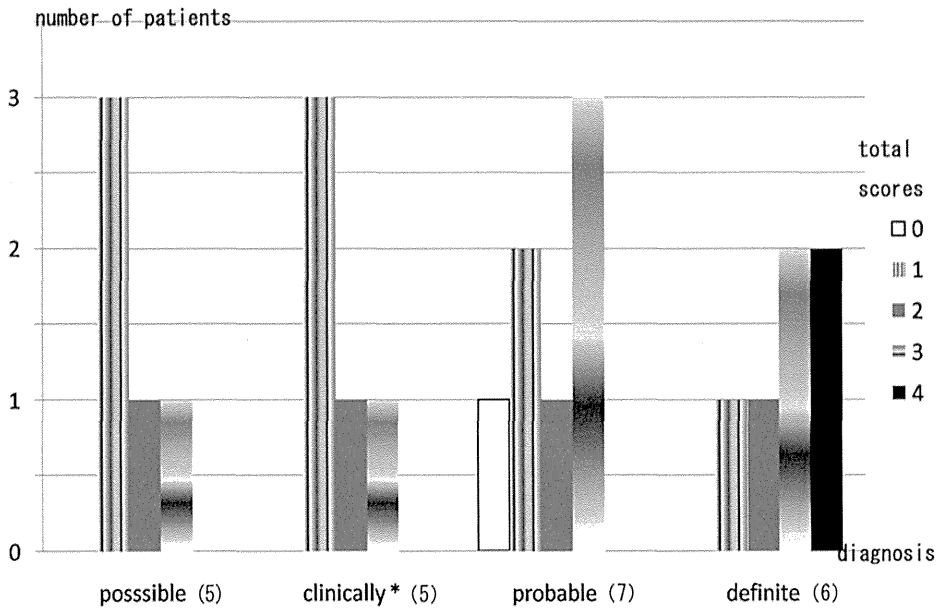

Fig 5. Relation between the certainty in the ALS diagnosis criteria and the signal intensity score on SWI. The scores of signal intensity might be roughly proportional to certainty in ALS diagnosis. Score '4' was found only in the group of patients diagnosed with definite ALS (n = 5).*clinically: clinically probable laboratory-supported ALS.

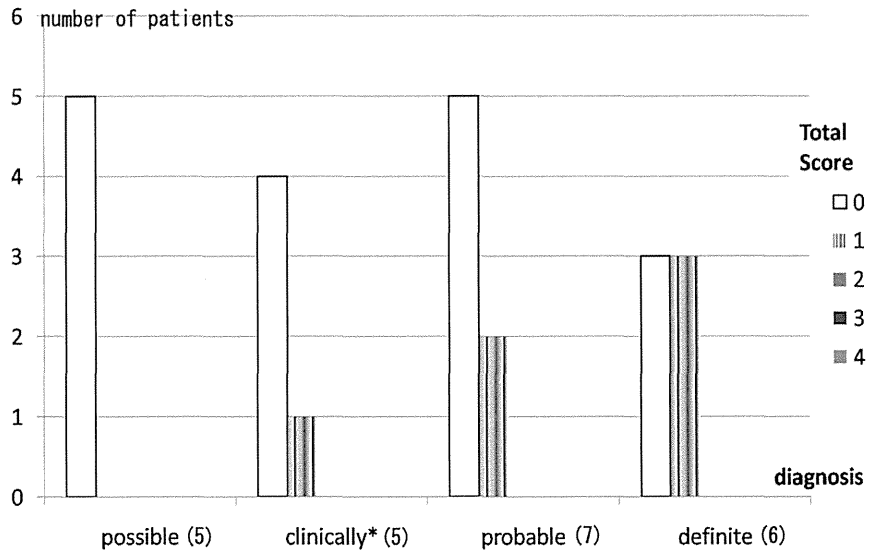

Fig 6. Relation between the certainty in the ALS diagnosis and the signal intensity score on T2-weighted image. The scores of signal intensity might be roughly proportional to the certainty in the ALS diagnosis. All possible ALS patients (n = 5) had total scores of 0 on T2-weighted images.

Figures 5 and 6 showed that the scores of signal intensity tended to be roughly proportional to the certainty of the ALS diagnosis on both SWI and conventional T2-weighted images. No remarkable correlation was found between the certainty of the diagnosis and signal intensity score on T2*-weighted images. The total score of '4' was found only in the group of patients diagnosed with definite ALS in Figure 5.

Figures 7 and 8 showed the breakdowns between the age groups and the SWI findings for the patients and normal controls, respectively. The total scores of the signal intensities of the precentral cortex were independent of age in the patients with ALS (Fig 7), whereas in the control group, age was positively associated with the grade of the precentral cortex (Fig 8). Figure 8 shows that score 1 and higher score was observed in no normal control subjects under age 50, and score 2

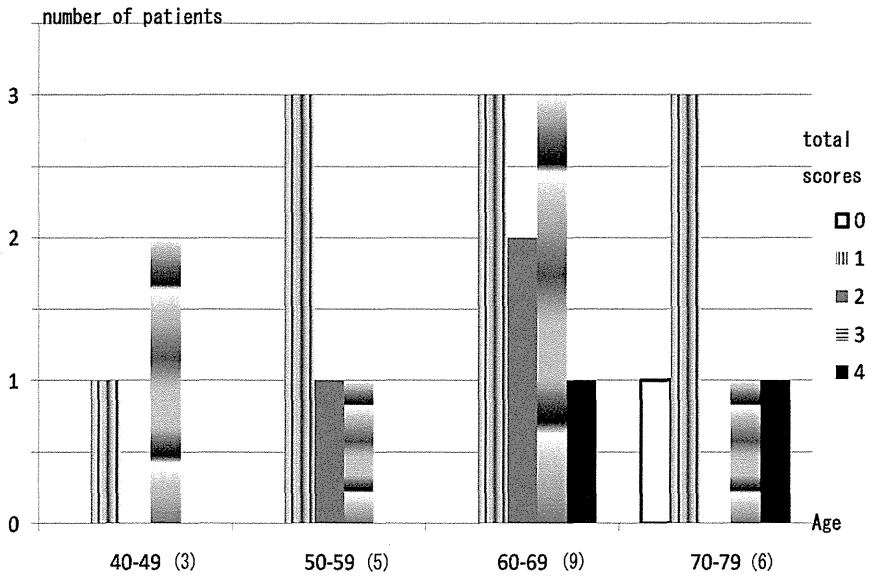

Fig 7. The total scores on SWI of the ALS patients ($n = 23$) in each age group. The vertical axis shows the total scores of the precentral cortex. The horizontal axis shows the patient age groups. There was no correlation between the total SWI score and age in the ALS patients.

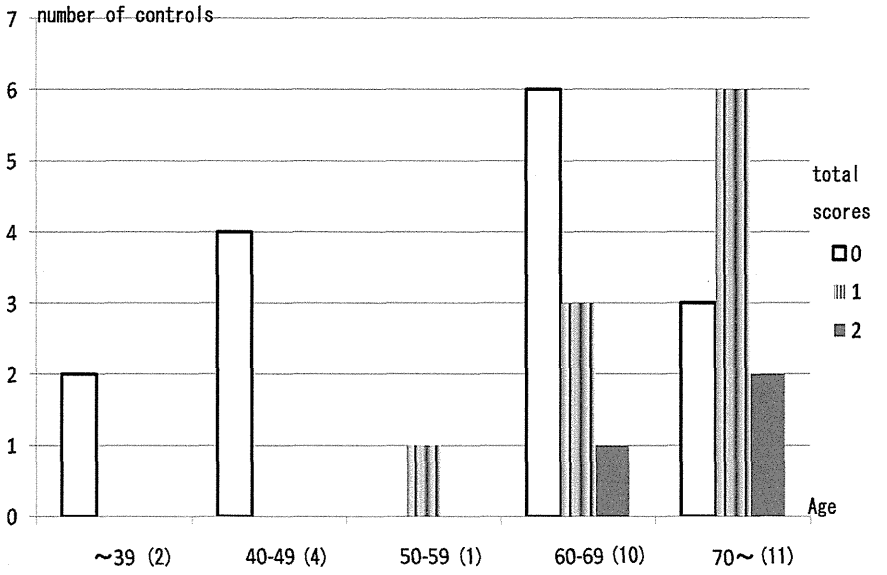

Fig 8. The total scores on SWI of the normal controls ($n = 28$) in each age group. The vertical axis shows the total scores of the precentral cortex, and the horizontal axis shows the age groups. The total scores of the signal intensities of the precentral cortex were positively correlated with age in the normal controls.

and higher score was measured only in elder normal controls over 60 years.

Statistical Analysis

Our stastistical analysis showed that the total scores of precentral cortical signal intensity on SWI in the ALS patients were significantly higher than those of the normal controls ($P < .0001$). There was no significant difference between the total scores of the patients and those of the controls on conventional spin-echo T2-weighted images or on T2*-weighted images. A significant correlation was shown between the precentral cortical signal intensity on SWI and age in the normal controls ($r = .494$). However, there was no such correlation in the ALS patients ($r = .012$). In the ALS group, no significant relationship was observed between the imaging score on SWI and disease duration ($r = .093$).

Postmortem Study

Pathological findings were obtained in a patient who died due to respiration failure at 67 years of age (Fig 4). His disease

duration was 2 years and 6 months. The time interval between the MR study and the postmortem examination was 4 months. Although the clinical symptoms were right-dominant due to LMN involvement throughout the course of the disease, physical examination could not prove right-dominant UMN involvement because of the patient's severe muscular atrophy. The patient had a score of 2 on the left on both the superior and inferior slices on SWI; thus, the total score was 4 (Fig 4A).

In the postmortem brain, the section taken from the precentral cortices showed intensely stained microglias and macrophages after antiferritin antibody staining compared to an age-matched normal brain (Fig 4D, E). The left precentral cortex was stained more strongly than the other side, which was compatible with MR images. However, hemosiderin deposition was found to be slightly stronger in this ALS patient than in the normal control by Berlin blue staining (data not shown); there was of a less significant difference between the patient and controls regarding Berlin blue staining compared to the difference in antiferritin antibody.

Discussion

To the best of our knowledge, this study is the first to focus on the ability of SWI to determine the precentral cortical signal intensity in ALS patients. Our findings demonstrate that SWI was a more sensitive sequence for detecting the low signal intensity of the precentral cortex in ALS patients than conventional T2-weighted and T2*-weighted images. This study also indicated better visualization of low signal intensity in the motor cortex with conventional spin-echo T2-weighted imaging than with T2*-weighted imaging. These results and the postmortem study suggested that the cause of low signals in the motor cortex may be the deposition of ferritin, which is a specific form of iron found in some neurodegenerative diseases.

Several reports providing the radiological findings of ALS patients have been published. The presence of low signal intensity in the motor cortex and high signal intensity in the pyramidal tract on T2-weighted images and the presence of atrophy of the motor cortex have been observed in ALS patients by conventional MRI techniques.[3,4] However, these findings are nonspecific in older patients and commonly absent in the early phases of the disease. Subsequently, some studies using advanced techniques including MR spectroscopy, diffusion tensor imaging and magnetization transfer imaging have advocated the usability of MRI to evaluate the corticospinal tract in ALS patients.[9–14] Recently, higher magnetic fields and the development of T2-weighted gradient techniques have allowed the detection of ferritin in narrow areas like the motor cortex.[26] We focused on the detection of ferric iron in the motor cortices of ALS patients using a standard magnetic field and generalized technique and suggested the clinical utility of MRI in the diagnosis of ALS.

The form of iron that binds with protein is important to diagnosis because the effects of ferritin in MR imaging are different from those of other binding forms of iron such as hemosiderin. Oba et al performed a Perls stain analysis of the postmortem brains of eight ALS patients to evaluate the ferric iron content in the motor cortex.[3] In three of the brains, the analysis revealed that the intensely stained astrocytes and macrophages that were sparsely distributed in the precentral cortices contained large amounts of ferric iron. In the present postmortem examination, the precentral cortex showed intensely stained microglias and magrophages after antiferritin antibody staining (Figs 4D, E) compared to age-matched normal brains (data not shown). Berlin blue staining, which reveals hemosiderin, showed almost the same staining between an ALS patient and the normal brain, indicating that decreased intensity of the motor cortex on SWI and T2-weighted image may represent ferritin.

It is known that the diagnosis of UMN involvement in ALS patients is not easy. The UMN involvement might be too subtle to detect by neurophysiological examination in the early stage of the disease, and the UMN involvement can be masked by extreme LMN impairment in the end stage.[1,2] Thus, detection of the UMN involvement by an imaging tool could be useful in ALS diagnosis. In our postmortem patient, the clinical symptoms caused by LMN involvement were right-dominant throughout the course of the disease, but it was difficult to evaluate UMN laterality because of the patient's severe muscle atrophy. His SWI showed left-dominant low signal intensity of the precentral cortices and his pathology presented left-dominant ferric deposition. This result suggested that SWI would be useful to detect neuronal degeneration in ALS patients. But 7 patients who had laterality in their UMN involvement did not show significant laterality on MR examination. This result might also be caused by the large variety of pathological findings, including the amount of iron in the motor cortex of ALS patients.

Ferritin is deposited in the gray matter with aging and in various neurological disorders such as Parkinson's disease, Alzheimer's disease (AD), multiple sclerosis, and ALS.[27–30] In contrast, hemosiderin is often deposited in the brain by other diseases such as cavernous hemangioma, amyloid angiopathy, and hemorrhagic infarction.[19,20,31] The detection of ferritin might be more important than that of hemosiderin when evaluating certain neurodegenerative diseases. It is well known that hemosiderin-containing areas in the brain tissue demonstrate more prominent hypointensity on T2*-weighted images than on T2-weighted conventional spin-echo and fast spin-echo sequences, due to magnetic susceptibility effects. However, Haque et al reported that conventional T2-weghted spin-echo images might be a better sequence to detect ferritin-containing areas than T2*-weighted and T2-weighted fast spin-echo images.[22] The molecular characteristics of ferritin and hemosiderin, regarding cluster size and intracellular distribution, have different effects in MR images.[31] Ferric iron is thought to form small clusters and distribute uniformly, whereas hemosiderin iron is insoluble and aggregated into irregular micron-sized clusters larger than ferritin. Haque et al described that uniform distribution of small ferritin granules produced field inhomogeneity causing T2-hypointensity, but minimal susceptibility difference leading to less pronounced hypointensity on T2*-weighted images.[22] In a previous study, decreased signal intensity was detected in most of ALS patients (93%, 14/15) on conventional T2-weighted images.[3] Although this result looked conflict with ours (low signal was detected in 6/20, 30%), it assumed to be due to the difference of the evaluation method. Oba et al evaluated the motor cortex using three directions including the top of the cerebral hemisphere. Whereas, we used

just two slices in order to avoid the artifact from head surface on gradient sequences.

SWI was the most sensitive sequence to detect the low signal intensity of precentral cortices in ALS patients. Although SWI is basically a gradient echo sequence like T2*-weighted imaging, the combination of the phase and the magnitude information creates new images with a unique contrast, different from that of T2*-weighted images. This combination takes full advantage of magnitude and phase information to highlight both types of contrast on one sequence.[19] The tissues containing a very small amount of iron with uniform distribution would change SWI phase, but influence little T2* effect. SWI is an appropriate sequence to reflect the changes in phase images caused by small amounts of magnetic substance deposition.[19,32–34] A previous study described that T2*-weighted images provide superior contrast compared to T2-weighted images (fast spin-echo) to detect amyloid plaque in AD, but SWI provides the greatest contrast.[35] It has been postulated that the contrast of amyloid plaques in AD patients is due to the accumulation of iron as is the case with motor cortices in ALS. They also calculated the T2 and T2* values of plaque and these values were similar; therefore, the authors concluded that the iron concentration in the plaques is not as great as previously thought. This result supports that SWI might be the most appropriate sequence to visualize small amounts of iron, especially ferritin.

In the control group, a correlation was shown between age and the decreased signal intensity of the motor cortex on SWI. No such correlation was found in the ALS group. These results indicate that SWI might be appropriate sequence to detect pathological (not physiologic) ferric iron which is deposited on the brain in some kinds of neurodegenerative diseases. Particularly, low signal intensity of motor cortex in young patients suspected ALS is diagnostic value because ferric iron deposition is not common in normal condition in the youth.

Some limitations of this study need to be acknowledged. First, we visually evaluated the signal intensity of the motor cortex. Recent studies have shown various approaches to the measurement of brain iron on SWI.[36–40] However, many of these studies focused on deep gray matter, not on the motor cortex. The air-to-tissue and/or the fat-to-skull interfaces cause large enough susceptibility artifacts to make SWI- and GRE-based methods impractical for quantitative evaluation of motor cortices. Thus, we selected visual assessment because the motor cortex is a thin linear structure located in surface of the cerebral hemisphere on which it is difficult to specify a region of interest (ROI). Liu et al have been challenging to apply Quantitative Susceptibility Mapping (QSM) to motor cortex in ALS patients as a biomarker (Lie et al unpublished data). They showed that the statistically significant deference of the mean susceptibility between the ALS patients and controls. Although quantitative methods expected as a biomarker in the future, further studies are needed. Second, we evaluated data obtained using a 1.5-T MR system. However, higher magnetic field MR systems, such as a 3-T MR unit, could produce better findings in terms of signal-to-noise ratio (SNR), acquisition times, and clear anatomical coverage.[26,41] Kwan et al showed decreased signal intensity in the motor cortex of ALS patients on both 3-T fluid-attenuated inversion recovery (FLAIR) and 7-T gradient images.[26] Although ferric iron detection might be difficult on T2*-weighted and T2-weighted fast spin echousing 1.5-T MRI, a high magnetic field and more sensitive sequences such as SWI have the potential ability to accurately detect ferritin. Third, evaluation of the UMN involvement was not completed. We should have taken particlar note of the UNM laterality as clinical information because our study focused on motor cortices which reflect UMN changes. However, it is known that as the disease progresses, increasing LMN impairment can conceal UMN involvement, and in some cases, even disguise a reversal of UMN laterality. As another limitation of the present study, the heterogeneity of the diagnostic certainty of the ALS; patients diagnosed with definite ALS to possible ALS were included. This could make the decreased signal intensity of the motor cortex not necessarily correlated with the clinical symptoms and disease duration. However, we found that decreased signal intensity was obvious in the patients diagnosed with definite ALS (Fig 5). The signal intensity scores tended to be roughly proportional to the certainty of the ALS diagnoses.

Conclusions

We concluded that low signal intensity in the motor cortex of ALS patients might reflected iron deposition, and SWI was the most sensitive MR sequence to detect it. T2*-weighted imaging has been considered a useful sequence for detecting intracranial iron, but conventional spin-echo T2-weighted imaging is superior to T2*-weighted imaging for detecting ferritin. SWI might be the most appropriate sequence to detect ferric iron and useful for diagnosis of ALS, especially in the younger patients.

References

1. Benatar M. *Neuromuscular Disease: Evidence and Analysis in Clinical Neurology.* Totowa, New Jersey: Humana Press Inc, 2006:43-58.
2. Lerner AJ. *Diagnostic Criteria in Neurology.* Totowa, New Jersey: Humana Press Inc, 2006:183-191.
3. Oba H, Araki T, Ohtomo K, et al. Amyotrophic lateral sclerosis: T2 shortening in motor cortex at MR imaging. *Radiology* 1993;189:843-846.
4. Agosta F, Pagani E, Petrolini M, et al. MRI predictors of long-term evolution in amyotrophic lateral sclerosis. *Eur J Neurosci* 2010;32:1490-1496.
5. Chan S, Shungu DC, Douglas-Akinwande A, et al. Motor neuron diseases: comparison of single-voxel proton MR spectroscopy of the motor cortex with MR imaging of the brain. *Radiology* 1999;212:763-769.
6. Govind V, Sharma KR, Maudsley AA, Arheart KL, et al. Comprehensive evaluation of corticospinal tract metabolites in amyotrophic lateral sclerosis using whole-brain 1H MR spectroscopy. *PLoS One* 2012;7:e35607.
7. Agosta F, Pagani E, Petrolini M, et al. Assessment of white matter tract damage in patients with amyotrophic lateral sclerosis: a diffusion tensor MR imaging tractography study. *AJNR Am J Neuroradiol* 2010;31:1457-1461.
8. Wang S, Poptani H, Bilello M, et al. Diffusion tensor imaging in amyotrophic lateral sclerosis: volumetric analysis of the corticospinal tract. *AJNR Am J Neuroradiol* 2006;27:1234-1238.
9. Canu E, Agosta F, Riva N, Sala S, et al. The topography of brain microstructural damage in amyotrophic lateral sclerosis assessed using diffusion tensor MR imaging. *AJNR Am J Neuroradiol* 2011;32:1307-1314.

10. Cirillo M, Esposito F, Tedeschi G, Caiazzo G, et al. Widespread microstructural white matter involvement in amyotrophic lateral sclerosis: a whole-brain DTI study. *AJNR Am J Neuroradiol* 2012;33:1102-1108.
11. Sarro L, Agosta F, Canu E, Riva N, et al. Cognitive functions and white matter tract damage in amyotrophic lateral sclerosis: a diffusion tensor tractography study. *AJNR Am J Neuroradiol* 2011;32:1866-1872.
12. Carrara G, Carapelli C, Venturi F, Ferraris MM, et al. A distinct MR imaging phenotype in amyotrophic lateral sclerosis: correlation between T1 magnetization transfer contrast hyperintensity along the corticospinal tract and diffusion tensor imaging analysis. *AJNR Am J Neuroradiol* 2011;33:733-739.
13. Welsh RC, Jelsone-Swain LM, Foerster BR. The utility of independent component analysis and machine learning in the identification of the amyotrophic lateral sclerosis diseased brain. *Front Hum Neurosci* 2013;10:251.
14. Turner MR, Modo M. Advances in the application of MRI to amyotrophic lateral sclerosis. *Expert Opin Med Diagn* 2010;4:438-496.
15. Sharma KR, Sheriff S, Maudsley A, et al. Diffusion tensor imaging of Basal Ganglia and thalamus in amyotrophic lateral sclerosis. *J Neuroimaging* 2013;23:368-374.
16. Koennecke HC. Cerebral microbleeds on MRI: prevalence, associations, and potential clinical implications. *Neurology* 2006;66:165-171.
17. Kim JK, Kucharczyk W, Henkelman RM. Cavernous hemangiomas: dipolar susceptibility artifacts at MR imaging. *Radiology* 1993;187:735-741.
18. Atlas SW, Mark AS, Grossman RI, et al. Intracranial hemorrhage: gradient-echo MR imaging at 1.5 T. Comparison with spin-echo imaging and clinical applications. *Radiology* 1988;168:803-807.
19. Haacke EM, Mittal S, Wu Z, et al. Susceptibility-weighted imaging: technical aspects and clinical applications, part 1. *AJNR Am J Neuroradiol* 2009;30:19-30.
20. Nandigam RN, Viswanathan A, Delgado P, et al. MR imaging detection of cerebral microbleeds: effect of susceptibility-weighted imaging, section thickness, and field strength. *AJNR Am J Neuroradiol* 2009;30:338-343.
21. de Souza JM, Domingues RC, Cruz LC, Jr., et al. Susceptibility-weighted imaging for the evaluation of patients with familial cerebral cavernous malformations: a comparison with t2-weighted fast spin-echo and gradient-echo sequences. *AJNR Am J Neuroradiol* 2008;29:154-158.
22. Haque TL, Miki Y, Kanagaki M, et al. MR contrast of ferritin and hemosiderin in the brain: comparison among gradient-echo, conventional spin-echo and fast spin-echo sequences. *Eur J radiol* 2003;48:230-236.
23. Brooks BR, Miller RG, Swash M, et al. World Federation of Neurology Research Group on Motor Neuron Diseases.El Escorial revisited: revised criteria for the diagnosis of amyotrophic lateral sclerosis. *Amyotroph Lateral Scler Other Motor Neuron Disord* 2000;1:293-299.
24. Iwasaki S, Nakagawa H, Fukusumi A, et al. Identification of pre- and postcentral gyri on CT and MR images on the basis of the medullary pattern of cerebral white matter. *Radiology* 1991;179:207-213.
25. Adachi T, Saito Y, Hatsuta H, et al. Neuropathological asymmetry in argyrophilic grain disease. *J Neuropathol Exp Neurol* 2010;69:737-744.
26. Kwan JS, Van Gelderen P, Deng HX, et al. Iron accumulation in deep cortical layers accounts for MRI signal abnormalities in ALS: correlating 7 tesla MRI and pathology. *PLoS One* 2012;7:e35241.
27. Vymazal J, Righini A, Brooks RA, et al. T1 and T2 in the brain of healthy subjects, patients with Parkinson disease, and patients with multiple system atrophy: relation to iron content. *Radiology* 1999;211:489-495.
28. Jellinger KA. The role of iron in neurodegeneration: prospects for pharmacotherapy of Parkinson's disease. *Drugs aging* 1999;14:115-140.
29. Qian ZM, Wang Q. Expression of iron transport proteins and excessive iron accumulation in the brain in neurodegenerative disorders. *Brain Res Brain Res Rev* 1998;27:257-267.
30. Swaiman KF. Hallervorden-Spatz syndrome and brain iron metabolism. *Arch Neurol* 1991;48:1285-1293.
31. Bakshi R, Shaikh ZA, Janardhan V. MRI T2 shortening ('black T2') in multiple sclerosis: frequency, location, and clinical correlation. *Neuroreport* 2000;11:15-21.
32. Wu EX, Kim D, Tosti CL, et al. Magnetic resonance assessment of iron overload by separate measurement of tissue ferritin and hemosiderin iron. *Ann N Y Acad Sci* 2010;1202:115-122.
33. Tao R, Zhang J, Dai Y, et al. An in vitro and in vivo analysis of the correlation between susceptibility-weighted imaging phase values and R2* in cirrhotic livers. *PloS One* 2012;7:e45477.
34. Haacke EM, Xu Y, Cheng YC, et al. Susceptibility weighted imaging (SWI). *Magn Reson Med* 2004;52:612-618.
35. Chamberlain R, Reyes D, Curran GL, et al. Comparison of amyloid plaque contrast generated by T2-weighted, T2*-weighted, and susceptibility-weighted imaging methods in transgenic mouse models of Alzheimer's disease. *Magn Reson Med* 2009;61:1158-1164.
36. Pfefferbaum A, Adalsteinsson E, Rohlfing T, et al. MRI estimates of brain iron concentration in normal aging: comparison of field-dependent (FDRI) and phase (SWI) methods. *Neuroimage* 2009;47:493-500.
37. Harder SL, Hopp KM, Ward H, et al. Mineralization of the deep gray matter with age: a retrospective review with susceptibility-weighted MR imaging. *AJNR Am J Neuroradiol* 2008;29:176-183.
38. Haacke EM, Miao Y, Liu M, et al. Correlation of putative iron content as represented by changes in R2* and phase with age in deep gray matter of healthy adults. *J Magn Reson imaging* 2010;32:561-576.
39. de Rochefort L, Brown R, Prince MR, et al. Quantitative MR susceptibility mapping using piece-wise constant regularized inversion of the magnetic field. *Magn Reson Med* 2008;60:1003-1009
40. de Rochefort L, Liu T, Kressler B, et al. Quantitative susceptibility map reconstruction from MR phase data using bayesian regularization: validation and application to brain imaging. *Magn Reson Med* 2010;63:194-206
41. Haacke EM, Makki M, Ge Y, et al. Characterizing iron deposition in multiple sclerosis lesions using susceptibility weighted imaging. *J Magn Reson imaging* 2009;29:537-544.

Journal of Cerebral Blood Flow & Metabolism (2014) 34, 1868–1872

www.jcbfm.com

ORIGINAL ARTICLE

Altered coupling of regional cerebral blood flow and brain temperature in schizophrenia compared with bipolar disorder and healthy subjects

Miho Ota[1], Noriko Sato[2], Koji Sakai[3], Mitsutoshi Okazaki[4], Norihide Maikusa[5], Kotaro Hattori[1], Hiroaki Hori[1], Toshiya Teraishi[1], Keigo Shimoji[2], Kei Yamada[6] and Hiroshi Kunugi[1]

Previous studies have suggested that schizophrenia patients have dysfunctional thermoregulation. The aim of this study was to examine whether brain temperature (BT) in schizophrenia patients differs from that in patients with bipolar disorder and healthy subjects by using magnetic resonance imaging. We also evaluated the possible relationship between BT and cerebral blood flow (CBF). We analyzed the temperature of lateral ventricles as the mean BT using diffusion-weighted imaging (DWI) thermometry, and evaluated the relationships between the BT and the CBF using pseudo-continuous arterial spin labeling (pCASL) among 3 diagnostic groups, 22 male patients with schizophrenia, 19 male patients with bipolar disorder, and 23 healthy male subjects. There were significant positive correlations between BT in the lateral ventricles and CBF in both the patients with bipolar disorder and healthy subjects. By contrast, there were significant negative correlations in patients with schizophrenia. We could not detect the significant difference in the surrogates of BT among three diagnostic groups. We showed that patients with schizophrenia, but not those with bipolar disorder, have dysfunctional thermoregulation in the brain. Brain temperature is highly dependent on cerebral metabolism and CBF, and thus uncoupling of cerebral metabolism and CBF may occur in schizophrenics.

Journal of Cerebral Blood Flow & Metabolism (2014) **34,** 1868–1872; doi:10.1038/jcbfm.2014.151; published online 3 September 2014

Keywords: arterial spin labeling; bipolar disorder; brain temperature; diffusion-weighted imaging thermometry; schizophrenia

INTRODUCTION

Schizophrenia is a psychotic disorder characterized by altered perception, thought processes, and behaviors; and bipolar disorder is a mood disorder involving prolonged states of depression and mania.[1] Historically, bipolar disorder and schizophrenia have been considered distinct nosological entities, with each disorder thought to have a different etiology and pathogenesis. However, the underling neural mechanisms of these disorders remain unclear. Functional brain imaging studies using positron emission tomography have most commonly reported that hyperdopaminergia are thought to be fundamental to the emergence of psychotic symptoms and to the mechanism of action of antipsychotics (for review, see Fusar-Poli and Meyer-Lindenberg[2]). Further, schizophrenia showed hypofrontality, a decrease in cerebral metabolic rate (CMR for glucose or oxygen) and a decrease in cerebral blood flow (CBF) in frontal regions revealed by positron emission tomography and single photon emission computed tomography (for review, see Hill *et al*[3]). However, increased prefronto-limbic CMR and CBF have been observed in some positron emission tomography and single photon emission computed tomography reports in bipolar disorder (for review, see Gonul *et al*[4]).

Cerebral metabolic rate and CBF have been found to be closely correlated in positron emission tomography studies in healthy human subjects.[4] However, some developmental, degenerative, ischemic, and neoplastic processes have been associated with an uncoupling of CMR and CBF.[5,6] Dunn *et al*[7] also showed the uncoupling of CMR and CBF in depressed patients. As for bipolar disease, they showed that patients with bipolar disease showed a positive correlation between CMR and CBF globally like controls.[7]

In healthy humans, brain temperature (BT) is determined by the balance between heat produced by cerebral energy turnover and heat removal.[8] Because heat removal is primarily dependent on CBF[8] and the arterio-venous temperature difference across the brain,[8,9] reduced cerebral perfusion relative to cerebral metabolism may indicate decreased central heat removal (i.e., higher BT).[10] Previous studies have suggested that schizophrenia patients have dysfunctional thermoregulation,[11–17] and these data suggest that patients with schizophrenia may exhibit abnormal BT.

Recently, human BT in lateral ventricle has been estimated noninvasively and accurately from the diffusion-weighted imaging

[1]Department of Mental Disorder Research, National Institute of Neuroscience, National Center of Neurology and Psychiatry, Kodaira, Tokyo, Japan; [2]Department of Radiology, National Center of Neurology and Psychiatry, Kodaira, Tokyo, Japan; [3]Department of Human Health Science, Graduate School of Medicine, Kyoto University, Sakyo-ku, Kyoto, Japan; [4]Department of Psychiatry, National Center of Neurology and Psychiatry, Kodaira, Tokyo, Japan; [5]Department of Imaging Neuroinformatics, Integrative Brain Imaging Center, National Center of Neurology and Psychiatry, Kodaira, Tokyo, Japan and [6]Department of Radiology, Graduate School of Medical Science, Kyoto Prefectural University of Medicine, Kamigyo-ku, Kyoto, Japan. Correspondence: Dr M Ota, Department of Mental Disorder Research, National Center of Neurology and Psychiatry, National Institute of Neuroscience, 4-1-1, Ogawa-Higashi, Kodaira, Tokyo 187-8502, Japan.
E-mail: ota@ncnp.go.jp
This study was supported by a Health and Labor Sciences Research Grant (for Comprehensive Research on Disability, Health, and Welfare) (MO and HK), an Intramural Research Grant (24-11) for Neurological and Psychiatric Disorders of NCNP (MO and HK), and a grant for 'Understanding of molecular and environmental bases for brain health' carried out under the Strategic Research Program for Brain Sciences by the Ministry of Education, Culture, Sports, Science, and Technology of Japan (HK).
Received 18 November 2013; revised 19 June 2014; accepted 29 July 2014; published online 3 September 2014

(DWI).[18,19] Cerebral blood flow can also be calculated noninvasively by pseudo-continuous arterial spin labeling (pCASL) imaging.[20] The aim of the present study was to examine whether the temperature of lateral ventricle, regarded as the mean BT, in schizophrenia patients differs from that in patients with bipolar disorder and healthy subjects by using DWI. We also evaluated whether there were differences in the relationship between BT and CBF among the three diagnostic groups by using pCASL.

MATERIALS AND METHODS

Subjects

Subjects were consisted of 22 male individuals with schizophrenia, 19 male individuals with bipolar disorder, and 23 healthy male subjects. Diagnosis was made according to the Diagnostic and Statistical Manual of Mental Disorders, 4th ed. (DSM-IV) criteria.[21] All subjects were Japanese males and biologically unrelated. The symptoms of all schizophrenia subjects were assessed by using the Positive and Negative Syndrome Scale (PANSS),[22] and the patients with bipolar disorder were rated with the 21-item Hamilton depression rating scale[23] and Young mania rating scale.[24] Daily doses of antipsychotics including depot antipsychotics and antidepressants were converted to chlorpromazine and imipramine equivalents using published guidelines, respectively.[25] The characteristics of the participants are shown in Table 1.

Healthy subjects were recruited from the community through local magazine advertisements and our website announcement. These participants were interviewed for enrollment by a research psychiatrist using the Japanese version of the Mini-International Neuropsychiatric Interview.[26] Participants were excluded if they had a prior medical history of central nervous system disease or severe head injury, or if they met the criteria for substance abuse or dependence. Those individuals who showed a history of psychiatric illness or contact with psychiatric services were excluded from the group of healthy subjects.

After the study was explained to each participant, written informed consent was obtained for participation. This study was approved by the ethics committee of the National Center of Neurology and Psychiatry, Japan.

Magnetic Resonance Imaging Data Acquisition and Processing

The magnetic resonance studies were performed on a 3-T MR system (Philips Medical Systems, Best, The Netherlands). The DWI was performed in the axial plane (repetition time/echo time, 5,760/62 ms; matrix, 80 × 80; field of view, 240 × 240 mm; 60 continuous transverse slices; slice thickness 3 mm with no interslice gap). To enhance the signal-to-noise ratio, acquisition was performed twice. Diffusion was measured along 15 noncollinear directions using a diffusion-weighted factor *b* in each direction of 1,000 s/mm^2, and one image was acquired without using any diffusion gradient. The imaging parameters for all of the pCASL experiments were single-shot gradient-echo echo planar imaging in combination with parallel imaging (sensitivity encoding (SENSE) factor 2.0), repetition time = 4,000 ms, echo time = 12 ms, matrix = 64 × 64, field of view = 240 × 240, voxel size = 3.75 × 3.75 mm, 20 slices acquired in ascending order, slice thickness = 7 mm, 1-mm gap between slices, labeling duration = 1,650 ms, postspin labeling delay = 1520 ms, time interval between consecutive slice acquisitions = 32.0 ms, radio frequency duration = 0.5 ms, pause between radio frequency pulses = 0.5 ms, labeling pulse flip angle = 18°, bandwidth = 3.3 kHz/pixel, echo train length = 35. Thirty-two pairs of control/label images were acquired and averaged. The scan duration was 4 minutes and 24 seconds. For measurement of the magnetization of arterial blood and also for segmentation purposes, an echo planar imaging M0 image was obtained separately with the same geometry and the same imaging parameters as the pCASL without labeling. Details of the calculation of regional CBF (rCBF) are described elsewhere.[19] The CBF maps were then normalized with the DARTEL (diffeomorphic anatomical registration using the exponentiated lie) registration method using a template made from the average CBF maps of healthy subjects previously recorded at our center.[27] Each map was then spatially smoothed with a 4-mm full-width at half-maximum Gaussian kernel to decrease spatial noise and compensate for the inexactitude of normalization.

Calculation of the Brain Temperatures

Diffusion-weighted imaging analysis. We extracted the body of the lateral ventricle and calculated the mean temperature in the lateral ventricle using the automated temperature calculation method.[19] In this method, the diffusion coefficient in the diffusion direction *i* was calculated by Equation [1] and then converted to a temperature.

$$D_i = \ln(S_o/S_i)/b \quad [1]$$

Here, D_i is the diffusion coefficient (mm^2/s) along the diffusion direction *i*, *b* is the applied diffusion weighting (s/mm^2), and S_0 and S_i are the voxel signal intensities of the reference and diffusion-weighted images along diffusion direction *i*, respectively. The D_i value was converted to the corresponding temperature using Equation [2].

$$T_i = (2256.74/\ln[4.39221/D_i]) - 273.15 \quad [2]$$

Here, T_i is in the unit of degrees Celsius (°C). The temperature within the lateral ventricle was determined according to our previous paper.[18]

Statistical Analysis

The differences in age and years of education among patient groups and healthy subjects were evaluated using analysis of variance, and the differences in age at onset and dose of antipsychotics and antidepressants were evaluated using two-sample *t* test. The differences of BT in lateral ventricles were evaluated using analysis of covariance controlling for age. The *post hoc* test was done using Bonferroni's correction for multiple comparisons. The correlations between BT in lateral ventricles and the clinical symptoms of disorders were evaluated using partial correlation

Table 1. Demographic and clinical characteristics of the subjects

Variable	*Healthy subjects*	*Schizophrenia*	*Bipolar disorder*	P
	Male (n = 23)	*Male (n = 22)*	*Male (n = 19)*	
	Mean ± s.d.	*Mean ± s.d.*	*Mean ± s.d.*	
Age (years)	39.3 ± 12.7	36.3 ± 10.4	42.4 ± 10.2	0.24
Education (years)	17.2 ± 4.0	14.8 ± 2.6	15.8 ± 3.3	0.06
Age at onset (years)		22.7 ± 6.1	32.7 ± 10.5	< 0.001
Antipsychotic medication[a] (mg/day)		573.9 ± 470.8	222.3 ± 344.5	0.01
Antidepressant medication[b] (mg/day)		38.0 ± 100.6	64.7 ± 141.4	0.5
HAM-D			12.2 ± 9.0	
Young mania rating scale			0.4 ± 1.1	
PANSS positive		14.8 ± 4.4		
PANSS negative		17.0 ± 7.3		
PANSS general		33.4 ± 10.2		

HAM-D, Hamilton's rating scale for depression; PANSS, positive and negative syndrome scale; s.d., standard deviation. [a]Chlorpromazine equivalent. [b]Imipramine equivalent.